Faculteit Industriële Ingenieurswetenschappen

master in de industriële wetenschappen: chemie

Masterthesis

Coating optimisation for fabrication of 3D printed electrodes used in hydrogen technologies

Tristan Geurts

Scriptie ingediend tot het behalen van de graad van master in de industriële wetenschappen: chemie

PROMOTOR :
Prof. dr. ir. Jozefien DE KEYZER

PROMOTOR :
dr. Vesna MIDDELKOOP

Gezamenlijke opleiding UHasselt en KU Leuven

UHASSELT KU LEUVEN

Universiteit Hasselt | Campus Diepenbeek | Faculteit Industriële Ingenieurswetenschappen | Agoralaan Gebouw H - Gebouw B | BE 3590 Diepenbeek

Universiteit Hasselt | Campus Diepenbeek | Agoralaan Gebouw D | BE 3590 Diepenbeek
Universiteit Hasselt | Campus Hasselt | Martelarenlaan 42 | BE 3500 Hasselt

UHASSELT KU LEUVEN

2024
2025

Faculteit Industriële Ingenieurswetenschappen

master in de industriële wetenschappen: chemie

Masterthesis

Coating optimisation for fabrication of 3D printed electrodes used in hydrogen technologies

Tristan Geurts

Scriptie ingediend tot het behalen van de graad van master in de industriële wetenschappen: chemie

PROMOTOR :

Prof. dr. ir. Jozefien DE KEYZER

PROMOTOR :

dr. Vesna MIDDELKOOP

UHASSELT KU LEUVEN

Preface

I would like to take a moment to thank the people whose support, encouragement and advice helped bring this thesis to completion.

First and foremost, I would like to express my gratitude to Vesna Middelkoop and Ahmet Can Kırlıoğlu for their excellent guidance and continuous support throughout the course of this master thesis. Their expertise and feedback made a significant impact on the development and execution of this work.

I would also like to thank my internal promotor at UHasselt/ KU Leuven, Josefien De Keyzer, for her valuable insights and encouragement, which helped me stay motivated.

A heartfelt thank you goes to my parents and sister, who have supported me unconditionally throughout my school career. Their belief in me helped me even during the most challenging moments.

Finally, I want to thank my friends and family for being there for me over the years. A special thank you goes to Brent Motmans, whose support, patience, and motivation meant a lot to me.

Table of Contents

List of Tables

List of Figures

Glossary of Terms

Alkaline Fuel Cells	(AFCs)	p.21
Area Specific Resistance	(ASR)	p.26
Artificial Intelligence	(AI)	p.15
Capital Expenditures	(CAPEX)	p.42
Design Of Experiments	(DOE)	p.40
Direct Current	(DC)	p.18
Direct Methanol Fuel Cells	(DMFCs)	p.21
Drops Per Inch	(DPI)	p.28
Electrochemical Impedance Spectroscopy	(EIS)	p.18
Electrochemically Active Surface Area	(ECSA)	p.16
Energy Dispersive X-ray Spectroscopy	(EDS)	p.17
Gadolinium Doped Ceria	(GDC)	p.18
Gas Diffusion Layers	(GDLs)	p.19
Hydrogen Oxidation Reaction	(HOR)	p.16
International Energy Agency	(IEA)	p.15
Isopropanol	(IPA)	p.28
Ketjenblack®	(KB)	p.16
Membrane Electrode Assembly	(MEA)	p.16
Molten Carbonate Fuel Cells	(MCFs)	p.21
Nickel Manganese oxide	(Ni-Mno)	p.27
One Factor At a Time	(OFAT)	p.38
Open-Circuit Potential	(OCP)	p.41
Operational Expenditures	(OPEX)	p.42
Oxygen Reduction Reaction	(OOR)	p.16
Particle Size Distribution	(PSD)	p.45
Phosphoric Acid Fuel Cells	(PAFCs)	p.21
Platinum	(Pt)	p.16
Polybenzimidazole	(PBI)	p.17
Proton Exchange Membrane Fuel Cells	(PEMFCs)	p.15
Pt in Ketjenblack®	(Pt/C)	p.33
Research & Development	(R&D)	p.29
Scanning Electron Microscopy	(SEM)	p.17
Solid Oxide Electrolysis Cells	(SOEC)	p.18
Solid Oxide Fuel Cells	(SOFCs)	p.15
Static Multiple Light Scattering	(SMLS)	p.34
Sulfonated Poly Ether Ether Ketone	(SPEEK)	p.23
Triple Phase Boundary	(TPB)	p.23
Turbiscan Stability Index	(TSI)	p.34
Yttria-Stabilized Zirconia	(YSZ)	p.24

Abstract

The transition to climate-neutral energy systems creates the need for efficient and cost-effective hydrogen-based electricity generation. Proton Exchange Membrane Fuel Cells (PEMFCs) are central to this transition, offering clean and direct conversion of green hydrogen into electricity. However, their scalability is hindered by reliance on platinum (Pt), an expensive and scarce catalyst. To optimise the Pt usage, four methods were compared for applying Nafion and Pt/C (carbon supported Pt) in water/IPA (2-propanol): jetting, hand spray coating (HSC), air spray coating (ASC) and ultrasonic spray coating (USC). The Pt/C coatings were applied onto 3D printed meshes, which offer high surface area, high conductivity and chemical durability. The electrodes, coated with an optimal (medium) loading of 0.77 mg_{Pt}/cm^2 were assessed for their coating uniformity and performance using optical microscopy, SEM, EDS and electrochemical testing. A maximum power density of 4.67 mW/cm^2 was achieved with ASC, but it used the most Pt during coating. The jetting coating resulted in the lowest performance (2.67 mW/cm^2) but was the most Pt-efficient. USC provided a balance between a maximum power density of 4.07 mW/cm^2 and a medium Pt usage for the coating. These results can help guide the selection of the optimal method for scaling-up depending on CAPEX and OPEX, electrode performance and efficiency as well as sustainability concerns.

Abstract in Dutch

De overgang naar klimaat neutrale energiesystemen maakt efficiënte en kosteneffectieve elektriciteit op basis van waterstof noodzakelijk. Proton Exchange Membrane Fuel Cells (PEMFC's) spelen een centrale rol in deze overgang, omdat ze groene waterstof op een schone en directe manier omzetten in elektriciteit. Hun schaalbaarheid wordt echter belemmerd door hun afhankelijkheid van platina (Pt), een dure en schaarse katalysator. Om het gebruik van Pt te optimaliseren, werden vier methoden voor het aanbrengen van Nafion® en Pt/C (Pt op koolstofdrager) formulaties in water/IPA met elkaar vergeleken: jetting, handspraycoating (HSC), luchtspraycoating (LSC) en ultrasone spraycoating (USC). De Pt/C inkt werden aangebracht op 3D geprinte gaasjes, die een groot oppervlak, hoge geleidbaarheid en chemische duurzaamheid bieden. De elektroden gecoat met een optimale belasting van 0,77 mg_{Pt}/cm^2, werden beoordeeld op hun coatinguniformiteit en prestaties met behulp van SEM, EDS en elektrochemische tests. Met LSC werd een maximale vermogensdichtheid van 4,67 mW/cm^2 bereikt, maar hierbij werd het meeste Pt gebruikt tijdens coaten. De jetting-coating leverde de laagste prestaties op (2,67 mW/cm^2), maar was het meest Pt-efficiënt. USC bood een evenwicht tussen een maximale vermogensdichtheid van 4,07 mW/cm^2 en een gemiddeld Pt-verbruik voor de coating. Deze resultaten kunnen helpen bij het kiezen van de optimale methode voor opschaling afhankelijk van CAPEX en OPEX, de performantie en efficiëntie van de elektroden en duurzaamheidsoverwegingen.

1 Introduction

1.1 Context

Addressing the increasingly rapid growth of the global energy demand with sustainable alternatives is an important challenge in the context of climate change. While non-renewable energy sources, such as petroleum, natural gas and coal, compensate for the current growth, their excessive use rapidly increases the amount of greenhouse gases in the atmosphere. Transitioning to renewable alternatives is therefore needed to reduce the carbon footprint of energy production. However, the output of renewable energy, such as wind and solar, is inherently fluctuating. To prevent a possible grid overload, excess renewable energy is currently curtailed, making grid stabilisation more important. Using hydrogen as an energy source, can mitigate the release of greenhouse gases while providing a solution to this problem. In peak times, renewable energy can be used to produce hydrogen. When more energy is needed, hydrogen can generate electricity, essentially providing a solution to the curtailment problem. In 2022, the International Energy Agency (IEA) reported that up to 6% of renewable energy in Europe was curtailed due to grid imbalances. This figure is expected to rise with the increase in percentage of renewable energy. With the future growth in power consumption through, for example Artificial Intelligence (AI), data centres, industrialisation, electrification and the projected increase in the world population over the next few decades, new, stable and sustainable green energy sources are desired [1], [2], [3], [4], [5].

Electrochemical energy storage and conversion technologies are emerging as key solutions to address the rising demand for stable and sustainable energy. Devices such as supercapacitors, fuel cells, and batteries have the potential to expand sustainable energy capacity, as they can convert and store green energy from renewable sources such as water, wind, solar, geothermal and biomass. [3], [6], [7].

Fuel cells convert the energy of a fuel, such as hydrogen or biogas, directly into electricity. The two most prominent types are the Solid Oxide Fuel Cells (SOFC) and Proton Exchange Membrane Fuel Cell (PEMFC). SOFCs have an overall higher working temperature of around 600 °C and are most efficient when excessive heat is used for electricity generation. PEMFCs have a lower operating temperature of around 70 °C while maintaining a higher overall efficiency (53-60%) than SOFCs (35-43%). For laboratory-scale experiments, SOFCs are less suitable due to their high operating temperature. Therefore, this research focuses on PEMFCs. The operation of a PEMFC is shown in Figure 1 [8], [9].

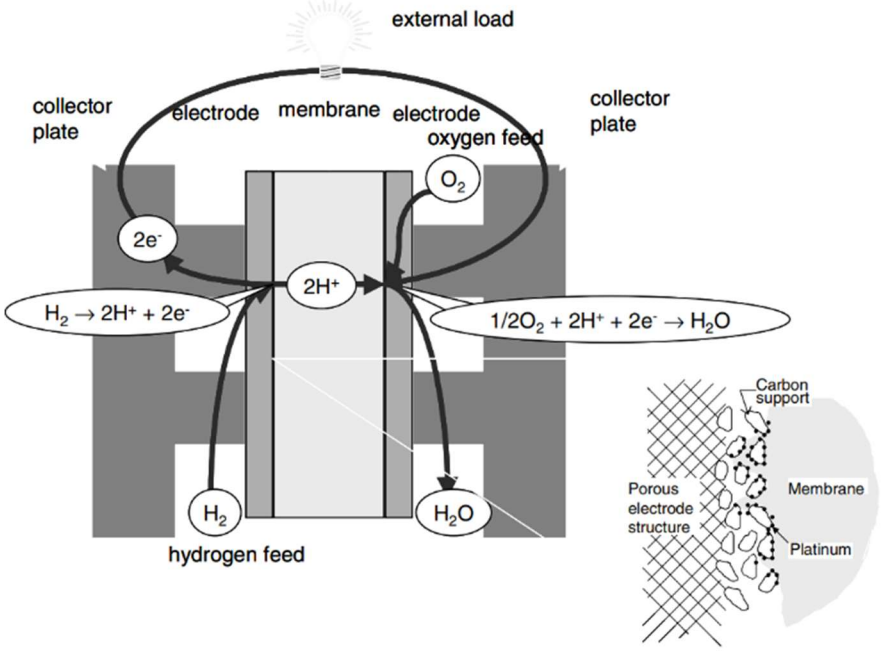

Figure 1: Electrochemical process in a PEMFC. Hydrogen splits into protons and electrons, protons pass through the membrane while electrons generate electricity via an external circuit [10, p. 41]

A Fuel Cell consists in general of two electrodes: anode and cathode. Both electrodes are typically coated with a thin carbon layer embedded with platinum (Pt) nanoparticles. Pt is used because of its exceptional catalytic activity in the electrolysis reaction. To maximise efficiency while minimising expensive Pt usage, the catalyst is typically made by depositing Pt nanoparticles onto a carbon support material. Conventional carbon black, such as Vulcan XC-72, has historically been used for this application as it provided a good structure for catalyst dispersion and electron transport within the electrode while providing a conductivity of 0.36 Ω·cm [10, p. 7911]. Recent advancements in electrode materials have led to the development of Ketjenblack® (KB), a conductive and porous carbon material. KB is a porous support structure, providing a large surface area of 1300 m²/g compared to the 250 m²/g for Vulcan XC-72. It has an excellent dispersion of Pt nanoparticles, which enhances the overall mass transport and electrochemical stability. Moreover, the dispersion increases the number of active catalyst sites and electron transport within the electrode. The improved intrinsic conductivity ranging from 0.01 to 0.1 Ω·cm helps to maintain catalyst accessibility while reducing electrode degradation compared to Vulcan XC-72 [11]. Overall, KB is preferred over the conventional carbon black for PEMFC electrodes due to higher activity and electrochemical stability but has a higher cost [12].

At the cathode, oxygen molecules react with the incoming protons and electrons to form water as a byproduct. The oxygen reduction reaction (OOR) shown in Equation 1.1, is slower compared to the hydrogen oxidation reaction (HOR), shown in Equation 1.2, making the cathode the rate-determining factor of the PEMFC performance.

$$H_{2(g)} \rightarrow 2H^+_{(aq)} + 2e^- \ (E^0 = 0.00\ V) \tag{1.1}$$

$$H_{2(g)} + \frac{1}{2}O_{2(g)} \rightarrow H_2O_{(l)} \ (E^0 = +1.23\ V) \tag{1.2}$$

The effectiveness of the catalytic layer is primarily influenced by the electrochemically active surface area (ECSA). The ECSA of a catalyst area depends on the Pt particle size and potential agglomeration which affect the overall performance of the fuel cell. Different additive manufacturing techniques, such as spray coating and inkjet printing, affect the final Pt particle distribution, which in turn influences the ECSA and potential agglomeration of Pt. Achieving a uniform, thin coating with sufficient active Pt loading while minimising material waste is the main objective of this thesis [9].

1.2 Problem statement

There are several challenges associated with the current coating processes of electrode layers in PEMFC. One major concern is the reliance on Pt as a catalyst, which significantly increases the cost of the cell. Pt accounts for approximately 91% of the total cost of the Membrane Electrode Assembly (MEA) [13]. The MEA itself represents 40-50% of the total PEM fuel cell cost [14, p. 10]. Another concern is material waste during the coating process, as inefficient deposition methods can lead to excess Pt usage, which increases production costs. Additionally, optimising the integration of different PEM cell components could further streamline manufacturing and enhance the efficiency [15], [16].

To make PEMFCs more viable, research is mostly focused on reducing the manufacturing costs of the MEA. Currently the standard used ionomer in the MEA for this application is Nafion® due to its high proton conductivity and important role as both a binder and ionic conductor in catalyst layers. Alternative membrane materials such as polybenzimidazole (PBI) are also being explored as substitutes with the aim of lowering costs and improving membrane durability. [17], [18], [19].

To improve the coating process and optimise material use, different additive manufacturing methods for electrode layer coating need to be evaluated. Various techniques, including spray coating, ultrasonic spray coating, hand spray coating, and jetting, offer different advantages and limitations. Spray and ultrasonic spray coating are widely used because of their ability to produce thin, uniform layers, although they may result in more material waste. Hand spray coating is more flexible for research applications but lacks consistency, making it more difficult to replicate experiments. Jetting, on the other hand, provides precise deposition with minimal waste but may be limited by viscosity and drying constraints. An optimal coating technique for this application has yet to be established, making it necessary to compare these techniques in terms of cost, scalability, and coating quality.

Therefore, this thesis is driven by the central question: Which electrode coating method provides the most efficient Pt loading while maintaining or improving the PEMFC performance, and what are the trade-offs regarding reproducibility, cost and scalability?

1.3 Objectives

The main objective of this project is to compare and evaluate different additive manufacturing techniques, such as jetting, ultrasonic spray coating, spray coating and hand spray coating for the development of an electrode layer in a PEMFC. These methods will be assessed on coating quality, efficiency of the Pt used, future scalability, desired thickness (2-30 μm) and fuel cell performance. The performance of a successfully coated electrode will be tested. Additionally, if time permits, the project will explore the use of these coating methods for a new application.

Several more specific objectives are required to achieve the main objective.

The first specific objective is to develop a stable water-based suspension containing Pt-supported KB that remains homogeneous for at least one week. This stability will be optimised by adjusting the mass fractions of solid particles, selecting suitable solvents, and incorporating additives (Nafion® or other ionomers) to enhance the dispersion and prevent sedimentation.

The second specific objective is to determine the most effective coating technique by comparing four different methods: spray coating, ultrasonic spray coating, hand spray coating, and jetting. These techniques will be evaluated based on their ability to produce coatings that are homogeneous, reproducible, and on their Pt usage. The method that delivers the best balance between coating quality and minimal material waste will be selected for further optimisation.

The third specific objective is to assess the coating quality through comprehensive characterisation techniques. An optimal coating should exhibit uniformity with no significant agglomeration. These characteristics are analysed using various techniques, such as optical microscopy and Scanning Electron Microscopy (SEM), Energy Dispersive X-ray Spectroscopy (EDS) and other relevant techniques to quantify the coating morphology, thickness and uniformity. Moreover, the performance of the electrode layers will be assessed using fuel cell performance testing.

Multiple challenges accompany this thesis. A major challenge is the limited period, as optimising the coating process and conducting detailed structural and electrochemical analyses require extensive testing. Techniques such as SEM, EIS, and I/V performance measurements require multiple days to complete.

The following chapters cover a more in-depth analysis of the methods, findings and implications of the coating work in this thesis. Chapter 2 presents an in-depth literature study on the working principles of fuel cells and compares various electrode fabrication techniques. Chapter 3 outlines the materials and methods used, including suspension preparation, coating processes and characterisation approaches. In Chapter 4, the optimisation of the ink suspension is described, followed by a comparative analysis of different coting techniques in terms of coating morphology, catalyst distribution and electrochemical performance. The chapter concludes with a critical evaluation of the quality of the coating, material efficiency, and economic feasibility. Finally, Chapter 5 summarises the key findings and discusses their relevance for future improvements in PEMFC electrode fabrication.

1.4 Complementary research

To complement the focus on PEMFCs, additional experiments were performed on Solid Oxide Electrolysis Cells (SOECs) to broaden the applicability of the optimised coating methods. Hydrogen fuel cells and electrolysers are considered similar electrochemical devices, operating as reverse processes: while fuel cells use hydrogen and oxygen gases as fuels and produce Direct Current (DC) electricity and water, electrolysers, in reverse, use DC electricity and water to produce (rather than use) hydrogen and oxygen gases. This similarity of the basic principles also concerns the cell components and their fabrication methods. Hence SOECs follow the reverse reaction of a SOFC, shown in Figure 2.

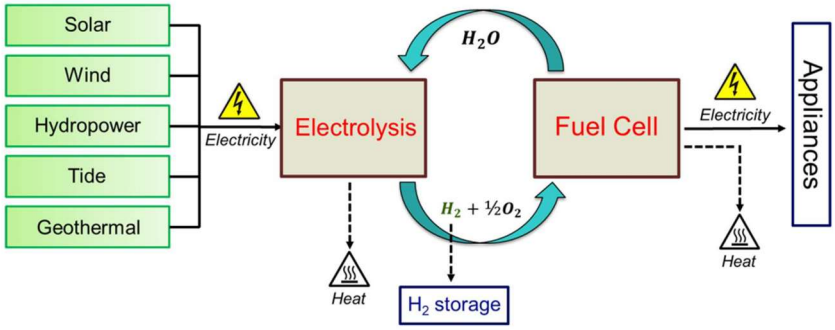

Figure 2: Schematic of the relation between the fuel cell and electrolysis cell for the production of green hydrogen [20, p. 3]

The technology holds the potential to address renewable energy curtailment by providing an efficient way to store chemical energy in the form of hydrogen. Equations 1.3 and 1.4 show respectively the cathode and anode reactions.

$$H_2O_{(l)} + 2e^- \rightarrow H_{2(g)} + O^{2-} \quad (E^0 = 0\ V) \tag{1.3}$$

$$2O^{2-} \rightarrow O_{2(g)} + 4e^- \quad (E^0 = +1.23\ V) \tag{1.4}$$

Given the similarity in the deposition of layers between PEMFCs and SOECs, this master's thesis investigates the feasibility of using ultrasonic spray coating and jetting for electrode deposition on SOEC substrates. The goal is to develop stable suspensions and evaluate coating morphology with Scanning Electron Microscopy (SEM) and electrochemical properties with Electrochemical Impedance Spectroscopy (EIS) and Arrhenius plots on Gadolinium-Doped Ceria (GDC) based electrolyte substrate. This is beneficial to explore the adaptability of the optimised deposition methods to different electrochemical systems.

2 Literature study

2.1 Fundamentals of fuel cells

2.1.1 Principles of fuel cells

Fuel cells are electrochemical devices that convert the chemical energy of a fuel, usually hydrogen, into electricity and heat. The chemically stored energy is converted directly into electricity through an electrochemical redox process, similar to a battery system. The main difference with a battery is that fuel cells can produce electricity continuously as long as fuel is supplied, while batteries require recharging [15]. Compared to other classic power systems, fuel cells function without moving parts and operate in a wider range of temperatures.

In classical power systems, the first step is to convert the chemical energy into heat using combustion. The heat is then converted into steam that powers a generator, used to generate electricity. However, in fuel cells, chemical energy is directly used to produce electricity, eliminating losses due to extra conversion processes [21]. The most common reaction of a fuel cell involves hydrogen and oxygen to generate electricity, with heat and water as by-products. When hydrogen is derived from renewable sources, the entire process has no negative impact on the climate, making it an attractive option for sustainable energy systems [22].

However, not all hydrogen methods are equally sustainable. Hydrogen is categorised by different colours that indicate the production method used. Grey hydrogen, for example, comes from fossil fuel reforming, which produces significant CO_2 emissions. Blue hydrogen, on the other hand, is made using natural gas reforming, combined with carbon capture technologies. Pink hydrogen uses nuclear-powered electrolysis that has low-carbon benefits, but it relies on nuclear energy. Both pink and blue hydrogen still have CO_2 emissions. This CO_2 can increase the greenhouse effect in the atmosphere, increasing the average temperature on the planet. In contrast, green hydrogen is produced by using renewable energy sources such as wind, solar or hydropower as fuel to electrolyse water into hydrogen without CO_2 emissions. PEMFCs and SOFCs are among the main technologies that can efficiently use green hydrogen as a clean energy source [23].

A fuel cell consists of several components that together convert chemical energy into electricity. The core component of the PEMFC is the MEA, which consists of the electrodes, Gas Diffusion Layer (GDL) and the membrane. To achieve higher power output, multiple MEAs are connected in series and placed between bipolar plates, forming a fuel cell stack. Figure 3 shows the structure of a typical fuel cell stack and the different components of one module.

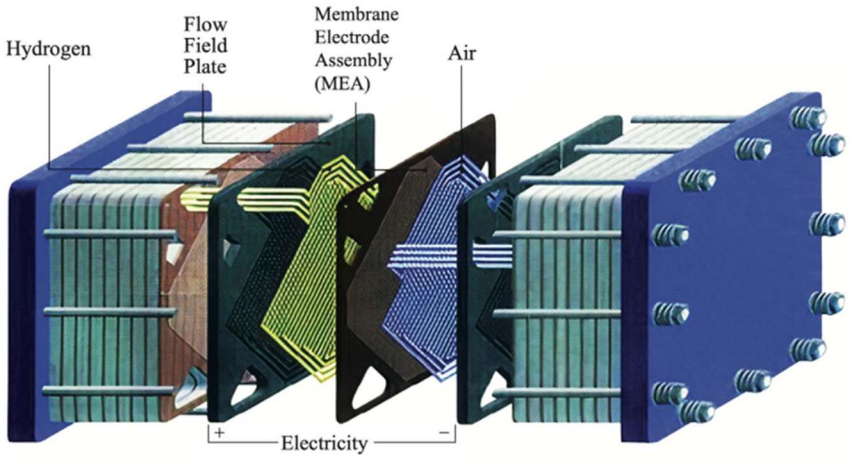

Figure 3: Layered structure of a PEM fuel cell, including flow field plates, MEA, and gas flow. [21, p. 372].

The fuel cell schematic, shown in Figure 3, illustrates a PEMFC. Hydrogen gas enters the fuel cell from the anode side, where it is distributed across the flow field plates. These plates ensure uniform gas distribution and remove excess water to prevent flooding, which improves efficiency. The hydrogen gas then interacts with the MEA, which is the core of the fuel cell. The different components, pressed together, are the membrane layer, catalyst-coated GDLs, a Gasket on both sides and two graphite flow fields, shown in Figure 4.

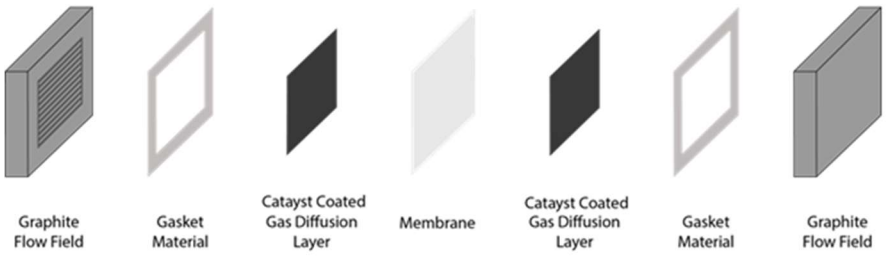

Figure 4: Illustration showing the different components of the MEA, adapted from [24]

The Graphite flow fields serve two purposes. First, they act as electrical conductors by collecting and transferring current generated by the electrodes. Second, they contain flow field channels that guide the gases (hydrogen and oxygen/air) across the surface of the MEA, ensuring efficient gas distribution and water management [25]. Next, the gasket is responsible for proper compression, alignment and sealing of MEA to prevent leaks. The catalyst-coated GDLs are situated outside the membrane layer and distribute the gases evenly during the reaction while Pt ionises the hydrogen atoms into protons and electrons. The inner layer, made from Nafion®, is the PEM. Here, the protons that were separated in the GDLs can migrate through the membrane while the electrons move through an external circuit, creating electricity. At the anode, Pt reacts again with oxygen gas to form hydroxides. Together with the protons from the membrane, hydroxides and protons together form water. The modular design allows for stacking of multiple cells, which improves scalability [26], [27].

Throughout history, various fuel cells with distinct characteristics have emerged. Lower temperature systems, such as Direct Methanol Fuel Cells (DMFCs), operate in the range of 70-130 °C and directly convert liquid methanol into electricity without the need for external reforming. The use of a liquid fuel such as methanol simplifies storage. However, their lower power density and slower reaction kinetics

limit their overall efficiency to around 20-30%. The most significant disadvantage of DMFCs is CO_2 as a byproduct, which mitigates the sustainable characteristic of fuel cells [28], [29], [30].

Alkaline Fuel Cells (AFCs), another low-temperature option, operate at around 70 °C and use an aqueous alkaline electrolyte to enable the rapid oxygen reduction reaction. The catalyst environment can be less corrosive, enabling the utilisation of more cost-effective catalysts, such as nickel. Despite this cost advantage, AFCs are highly sensitive to CO_2, which can form carbonates that poison the electrolyte and degrade performance, posing a major challenge. Moreover, while the alkaline environment is less corrosive to catalysts, it is still chemically aggressive to other components, requiring the use of corrosion-resistant cell materials, ultimately increasing the overall system cost. [28], [29].

PEMFCs have gained significant attention due to their quick startup time and efficient load-handling capabilities. Because of the high power-to-weight ratio combined with the lower operating temperature of 80 °C, the PEMFCs have been engineered for a wide range of applications, from mobile phones to locomotives [31]. However, their reliance on Pt as a catalyst raises the production cost. Pt accounts for approximately 45% of the total cell cost, and its scarcity remains a challenge to become the main competitor in the market [32].

Medium-temperature fuel cells such as Phosphoric Acid Fuel Cells (PAFCs) operate at temperatures ranging from 150-210 °C and use liquid phosphoric acid as the electrolyte, which has good efficiency in cogeneration applications. PAFCs, however, exhibit a relatively low power density, making them less suitable for space and weight-constraint applications. Furthermore, due to the significant amount of Pt and corrosion-resistant materials needed, the fuel cell is overall more expensive [28], [29].

For high-temperature applications, Molten Carbonate Fuel Cells (MCFs) are used that function through the utilisation of a molten carbonate electrolyte, which supports electrochemical reactions at high temperatures and makes it possible to convert a variety of fuels into electricity efficiently. MFCs typically operate around 600 °C. The most significant challenge associated with this technology pertains to its vulnerability to corrosion and the need for an advanced thermal management system [28], [30]. SOFCs, on the other hand, use a solid ceramic electrolyte that conducts oxide ions and operates at 600 °C. The fuel cells can manage multiple types of fuel and have an efficiency of up to 60%, and when combined with cogeneration, it rises to up to 85%. It is mostly used in industrialisation applications, as it has a long start up time. The high temperature has the added benefit of not needing a catalyst [28], [30].

Each type of fuel cell has specific advantages and disadvantages. However, due to their high efficiency and advanced development in various applications, SOFCs and PEMFCs are the most promising technologies and thus the focus of this paper.

2.1.2 Proton Exchange Membrane Fuel Cells

PEMFC is a widely researched fuel cell technology and works by using electrochemical reactions to convert the chemical energy of hydrogen into electricity. A core component of a PEMFC is the proton exchange membrane, which selectively allows protons to migrate while blocking electrons. Within the cell, hydrogen gas is supplied to the anode, where it undergoes oxidation, splitting into protons and electrons. The protons then migrate through the membrane, while the electrons travel through an external circuit, producing electrical power. At the cathode, oxygen reduces with the protons and electrons, forming water as the only by-product [31].

Within a PEMFC, the HOR occurs at the anode (Figure 1), Equation 2.1. While the ORR takes place at the cathode; Equation 2.2. The overall reaction combines hydrogen and oxygen to form water, Equation

2.3. The efficiency losses of these reactions arise due to overpotentials which are voltage losses caused by kinetic barriers, mass transport limitations, and internal resistance in the cell. In ideal circumstances, the reaction produces 1.23 V [33].

$$2H_{2(g)} \rightarrow 4H^{+}_{(aq)} + 4e^{-} \quad (2.1)$$

$$O_{2(g)} + 4H^{+}_{(aq)} + 4e^{-} \rightarrow 2H_2O_{(l)} \quad (2.2)$$

$$2H_{2(g)} + O_{2(g)} \rightarrow 2H_2O_{(l)} \quad (2.3)$$

Common losses with PEMFCs arise from the different energy barriers that are associated with the electrochemical reactions. Ohmic losses during the reaction are caused by resistance to ion flow through the membrane and electron flow through the electrode and external circuit. Mass transport losses occur when reactants are not supplied efficiently to the reaction site. As a result, real-world PEMFCs operate at voltages between 0.6 and 0.8 V under load [34], [35]. Figure 5 shows a common polarisation curve from a PEMFC, giving an overview of all the common losses at each current density.

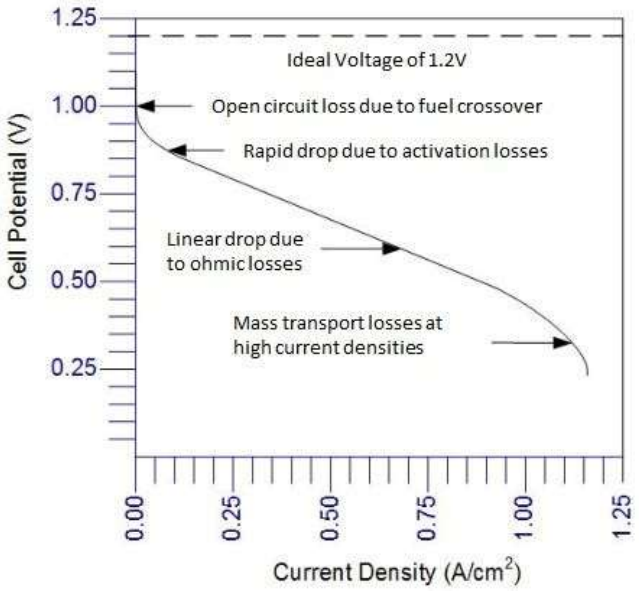

Figure 5: Polarisation curve of a PEMFC, showing the common losses at different current densities [36]

The low operating temperatures and high power density make this fuel cell the preferred option for applications ranging from portable electronics to transportation and small stationary power systems. Additionally, when supplied with green hydrogen, they produce zero emissions, making them a promising clean energy solution. However, commercial deployment faces challenges such as the excessive cost of Pt-based catalysts, durability limitations, and the need for effective water management within the cell [34], [35].

The MEA of the PEMFC consists of the GDL where hydrogen can penetrate the layer, the electrode with the catalyst and the proton exchange membrane where the protons can flow through. Other gases, such as air and CO_2 can also penetrate the GDL, creating the need for pure hydrogen sources during experiments. Through the electrode, hydrogen will interact with Pt, which catalyses the reaction by

lowering the activation energy, making it possible for the hydrogen to split into protons and electrons. The hydrogen protons move through the Nafion® membrane. The electrons get collected by the KB support and pushed through an external circuit where they produce electricity. Figure 6 shows the interaction between the GDL, electrode and proton exchange membrane.

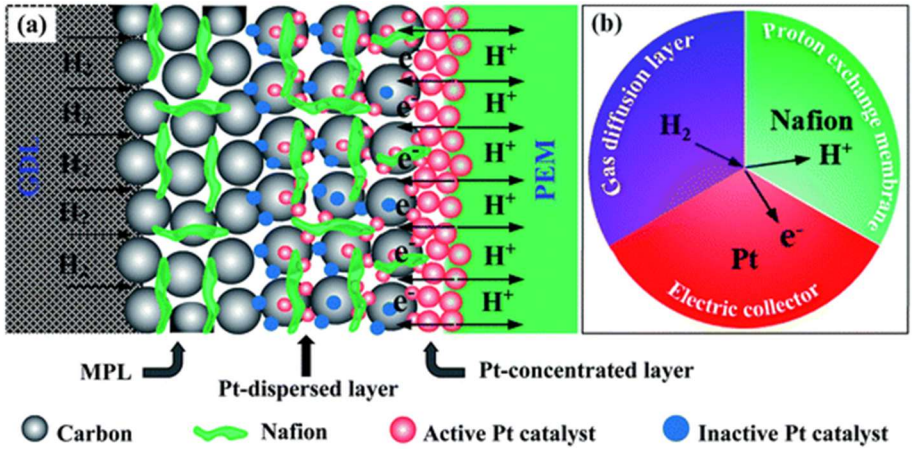

Figure 6: Schematic illustration showing the interaction of hydrogen with the GDL, the Pt-coated electrode and the Nafion® membrane on the left and the critical role of the triple phase boundary (TPB) on the right [37, p. 15640]

The Triple Phase Boundary (TPB) is an important microenvironment where three active components come together. Hydrogen gas from the GDL, active Pt catalyst particles supported on KB and the Nafion® proton exchange membrane. Here, hydrogen molecules are absorbed by the Pt particles where they split into protons (H^+) and electrons (e^-). The H^+ migrate through the hydrated Nafion® ionomer membrane while the e^- are conducted through the KB support into the external circuit to perform electrical work. The effective formation and distribution of the TPBs impact the overall ECSA. This is used to quantify the portion of Pt that is part of the catalytic reaction. Not all Pt contributes to the ESCA, as some parts are electronically isolated by being embedded too deeply within the KB matrix or insufficiently covered by Nafion®. Consequently, the ionisation cannot be fully complete as the TPB is not present Maximising the TPBs improves the fuel cell efficiency without raising the cost price as less Pt is needed [37].

Recent studies indicate that Sulfonated Poly Ether Ether Ketone (SPEEK) has become a promising alternative to the conventional choice, Nafion®, because of its high-temperature stability and higher durability [38]. At this moment, Nafion® remains the industry standard due to excellent proton conductivity. However, active research is being done to replace Nafion® with a cheaper alternative [39]. Current advancements have also focused on optimising cell components to enhance efficiency, longevity, and cost-effectiveness. l [31], [32], [34].

Rahman *et al*. reported the use of KB as a promising catalyst support material for PEMFC applications compared to conventional carbon black due to the high surface area, good conductivity, and strong electrochemical stability. Compared to traditional carbon black like Vulcan XC-72, with a surface area of 250 m^2/g, KB has an improved surface area of 1300 m^2/g while also having a more favourable porous structure. This improves the catalyst utilisation and slows degradation during working cycles. In contrast, carbon black catalysts suffer from carbon corrosion, catalyst agglomeration and detachment under stress, making it less favourable for this application [12].

2.1.3 Solid Oxide Fuel Cells

SOFCs offer a sustainable alternative for the conversion of a wide range of fuels into electricity with high efficiency. Unlike low-temperature fuel cells that rely on proton conduction, SOFCs operate at high temperatures (around 600 °C to 1000 °C). The electrolytes used in SOFCs are solid oxide electrolytes typically based on fluorite-structured materials like yttria-stabilized zirconia (YSZ) or scandia-stabilized zirconia that conduct oxygen ions (O^{2-}) from the cathode to the anode [40]. Figure 7 shows the mechanism in a Solid oxide fuel cell.

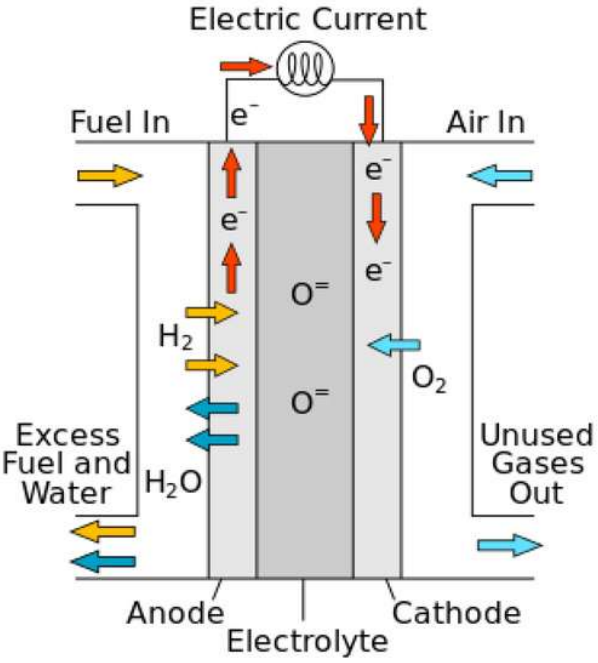

Figure 7: Operation of a SOFC, where oxygen ions migrate through a solid ceramic electrolyte to react with fuel at the anode [41, p. 3]

The cathode is typically made from strontium-doped $LaMnO_3$ as it has good stability at 1000 °C, a thermal expansion similar to YSZ and presents a good electrochemical activity for the reduction of oxygen, which occurs via Equation 2.4. At the anode, composite materials such as Ni/8YSZ or Ni/GDC are used as they provide both good electronic and ionic conductivity. These composites provide the anode with high activity for the electrochemical reactions and reforming that take place, while the mechanical characteristics also support the structure of the cell. The reaction at the anode is shown in Equation 2.5, and the overall reaction is shown in Equation 2.6 [9], [42], [43].

$$O_{2(g)} + 4e^- \rightarrow 2O^{2-} \tag{2.4}$$

$$H_{2(g)} + O^{2-} \rightarrow H_2O_{(l)} + 2e^- \tag{2.5}$$

$$H_{2(g)} + \frac{1}{2}O_{2(g)} \rightarrow H_2O_{(l)} \tag{2.6}$$

The high operating temperatures characteristic of SOFCs allow the use of non-precious metal catalysts, significantly reducing costs compared to lower-temperature systems. However, challenges such as

interfacial resistance, thermal cycling stability, and long-term degradation still need to be addressed to further enhance performance and durability [44]. Overpotentials arising from ohmic and polarisation losses and higher temperatures needed to perform this reaction remain factors that limit the overall efficiency [45]. When hydrocarbons are used as fuel, carbon deposits and sulphur may occur on the electrode, causing significant losses in performance even in concentrations under fifty parts per billion [9].

Overall, SOFCs offer promising prospects for sustainable energy conversion by harnessing high-temperature electrochemical processes. Recent developments in SOFC technology have also explored reversible operation, where the cell can function both as a fuel cell and an electrolyser. These advances involve tailoring electrolyte compositions and electrode architectures to balance high ionic conductivity with long-term stability under cyclic operating conditions, thereby enhancing the overall economic feasibility of SOFC-based energy systems [40], [44].

2.1.4 Conclusion

While SOFCs offer high efficiency and fuel flexibility when working at high temperatures, PEMFCs are better suited for fast lab-scale tests. However, the high cost of Pt group metals and durability challenges will have an impact on the fuel cell. By creating a more homogeneous coating, conductivity will improve, making way for advancing both SOFCs and PEMFCs research more sustainably. This thesis focuses on improving the deposition of Pt on the electrode of a PEMFC to reduce the amount of Pt needed without lowering activity by comparing multiple coating techniques.

In addition to the core focus on PEMFCs, the availability of in-house SOEC setup presented an opportunity to explore the adaptability of the optimised coating methods for developing electrodes for SOEC devices. To provide context for this additional research, SOECs are briefly introduced in the literature study.

2.1.5 Complementary research on Solid Oxide Electrolysis Cells

SOECs are high-temperature electrochemical devices. SOECs produce hydrogen through the reverse operation of a SOFC. These cells use renewable electricity to split water into hydrogen and oxygen at temperatures between 700 °C and 850 °C. These temperatures are important as they enable high ionic conductivity and fast kinetics.

In SOECs, the choice of electrolyte substrate is important. YSZ had long been the standard due to its thermal and ionic properties. However, at elevated temperatures, electrode elements such as strontium and cobalt diffuse into the YSZ substrate, leading to interface degradation. To combat this phenomenon, GDC was first used as a protective top layer but is now increasingly used as a full electrolyte support instead of just a barrier layer. GDC offers a high conductivity and increased chemical compatibility compared to YSZ, simplifying the overall cell construction.

To evaluate the electrode performance, from the complementary results, the activity of the SOEC electrodes coated on GDC electrolyte supports was analysed using EIS. A typical EIS measurement of a SOEC cell is presented in Figure 8.

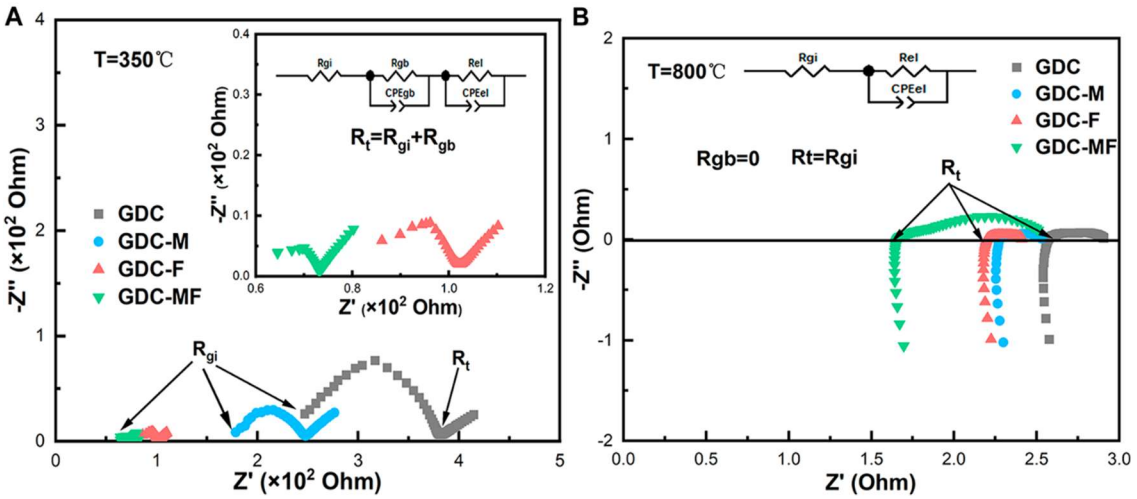

Figure 8: Typical EIS analysis of GDC-based electrolytes at 350°C (A) and 800°C (B) [46, p. 07]

This figure is called a Nyquist pot. The real part of impedance (Z`) is on the x-axis and the negative imaginary part (-Z``) is on the y-axis. The real impedance represents an ideal resistance while the imaginary impedance represents an ideal capacitor. Together, they form semicircles that correspond with an equivalent circuit model. Each semicircle corresponds to a resistance in the cell. The diameter of the semicircles indicates the resistance. The thicker, less uniform coating generally increases the overall resistance. In addition to hindering charge transport, excessive coating thickness can introduce internal mechanical stresses that may result in defects such as cracking. The figure shown above shows that the GDC-F and GDC-M samples have an overall lower resistance compared to the other samples, which is desirable. These results will be used to compare the results of the different coating methods [46].

In addition to impedance analysis, temperature-dependent electrochemical behaviour will be assessed using Arrhenius plots. According to the Arrhenius equation, the slope of this linear plot corresponds to the negative activation energy divided by the gas constant ($-E_a/R$). The y-axis represents the area-specific resistance (ASR). These ASR values are extracted from the EIS results by measuring the resistance of each semicircle, which corresponds with a different temperature. Figure 9 shows a typical Arrhenius plot for SOEC measurements.

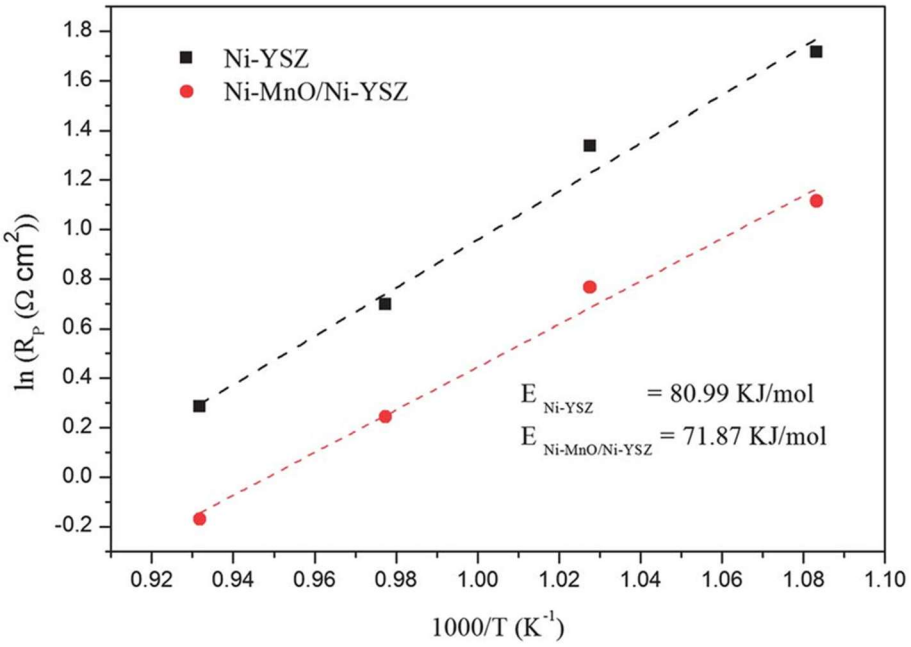

Figure 9: Example of a typical Arrhenius plot for Ni-YSZ and Ni-MnO/Ni-YSZ substrates [47, p. 1154]

The linear relationship in the Arrhenius equation allows for the extraction of the activation energy, which quantifies the minimum energy required to initiate the charge transport. A lower activation energy indicates a more efficient ionic conductivity or faster electrochemical kinetics, which is desirable for SOEC. By comparing the different slopes, assessments can be made regarding coating structure (porosity or particle contact) and reaction kinetics. In Figure 9 for example, adding Nickel Manganese oxide (Ni-Mno) lowers the activation energy, indicating improved electrochemical activity due to the addition of Mno. [47, p. 1154], [48]

2.3 Electrode fabrication techniques

Conventional fabrication techniques for the coating of the electrodes for PEMFC cells are dip coating, blading, brushing and casting. The most typical substrates that are used are carbon paper and metal mesh. The development and production of more efficient fuel cells with a lower cost remain important for advancing clean energy systems. One option for increasing the output of a fuel cell without increasing the price is improving the Pt deposition on the MEA, including highly porous 3D printed metal substrates (further referred to as 3D printed meshes). The performance of the MEA is dependent on the thickness, the Pt loading and how uniformly and homogeneously the coating is applied. A homogeneous coating improves the uniformity of the electrochemical reactions across the ESCA, reducing local inefficiencies while improving the durability of the fuel cell. Optimal coating is needed to balance the electrical conductivity with gas diffusion. If the layer is too thick, reactant transport is hindered. On the other hand, a layer that is too thin will lack sufficient catalytic activity. Similarly, Pt loading is important to maximise the catalyst usage while minimising material cost. Achieving this balance, however, is complicated by the limitations of the different coating methods.

Current coating methods, used for this application, face significant challenges, such as non-uniform distribution, poor control over the coating thickness and porosity, agglomeration of catalyst particles and excessive material waste. To improve the quality of the coating and select the most novel coating

technique for this application, this thesis compares four different coating methods that are used to produce Pt coating for MEAs. For each coating technique, different parameters such as homogeneous coating surface, coating thickness and loading impact will be tested and compared. Additionally, the Pt-coated MEAs will be tested in a fuel cell setup to find the most efficient technique for generating electricity.

2.3.1 Jetting

Material deposition through jetting has emerged as a versatile method for coating a catalyst layer on an electrode. This technique differentiates itself from others by using digitally controlled drop-on-demand ejection of catalyst inks. This way, nanodroplets containing Pt are placed precisely and spread evenly on the electrode [49]. The inkjet printing characteristic of jetting allows for more control over the architecture of the catalyst layer. This is important when minimising the Pt usage while maximising electrochemical performance. Jetting also enables more flexibility in the chosen pattern, which is useful for electrodes with a unique structure.

The process of jetting is becoming more promising, especially for coating Pt-infused KB catalysts. The success, however, is highly dependent on the optimisation of ink properties and machine coating parameters. Dao *et al.* created a similar ink with a viscosity in the range of 1-20 mPa·s and surface tension between 25 and 40 mN/m, which are optimal for stable jetting. These values minimise the issues, such as nozzle clogging and satellite droplet formation, commonly found in this technique [50, p. 41996]. These properties are achieved by choosing a solvent blend such as 2-propanol/water with the addition of surfactants or ionomers, such as Nafion®, which also helps with dispersing Pt nanoparticles and improving the amount of TPBs [37].

Beyond ink formulation, the optimisation of jetting parameters is important for achieving a uniform catalyst layer. Studies report the use of 500 and 1000 Drops per inch (DPI) for coating an electrode [51]. However, a current problem in inkjet printing is the coffee ring effect. This occurs during non-uniform evaporation, which causes particles to accumulate at the outside of the droplet, resulting in poor catalyst distribution and lower electrochemical activity. This phenomenon is driven by capillary flows inside a drying droplet but can be mitigated by adjusting the solvent composition and substrate temperature. Employing a mixed solvent such as isopropanol (IPA) and water, has been shown to suppress the coffee ring effect [52]. IPA has a lower surface tension, which introduces *Marangoni* flows that counteract the coffee ring formation while accelerating drying, as shown in Figure 10. Water, on the other hand, prevents overly rapid evaporation that can lead to nozzle clogging. Increasing the substrate temperature to typically 40 to 60 °C, minimises the capillary-driven particle migration [49], [53].

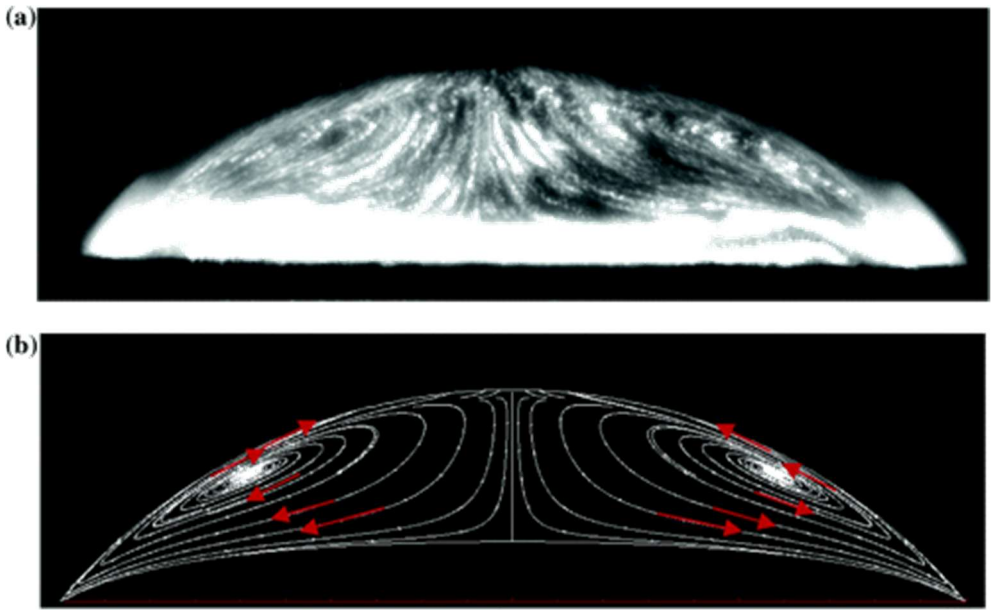

Figure 10: (a) showing the experimentally imaged Marangoni vortex in a droplet, (b) is a prediction of the flow pattern of the Marangoni vortex [53]

Because of the difference in surface tension, the *Marangoni* effect takes place. The vortex moves the particles in the suspension to prevent the particles from moving to the outside during evaporation, effectively minimising the coffee ring effect [53].

Bruijn *et al*. focused on the long-term behaviour of Pt-infused carbon electrodes and highlighted multiple issues such as Pt dissolution, carbon corrosion and ionomer degradation. The researchers focused on conventional fabrication methods, but their results showed that jetting is particularly promising for solving these problems. Using jetting, controlled placement of the nanoparticles can help mitigate the Pt migration or carbon support oxidation by optimising the layer thickness and uniformity. Furthermore, by optimising the catalyst distribution on known stress points, such as dry zones or high-voltage interfaces, more resilient and long-lasting electrodes can be produced [54].

While jetting is preferred for high precision and material efficiency, it presents multiple challenges such as ink sedimentation, nozzle clogging and droplet inconsistency. Current research is exploring real-time monitoring systems combined with closed-loop feedback control to improve the control over ink parameters to ensure consistent performance across multiple ink preparations. Furthermore, integrating AI and Machine Learning shows promise to improve the overall consistency of each layer [55].

2.3.2 Spray coating

Spray coating offers a cost-effective, scalable and controllable way to form a thin catalyst layer on a wide variety of substrates. In this process, a liquid precursor sprays fine droplets on a substrate. Here the droplets spread and form a uniform layer. Spray coating stands out for its ability to quickly coat large areas while maintaining control over coating thickness and morphology. In this part, multiple spray coating techniques will be explored with all their advantages and disadvantages [56].

2.3.3 Air spray coating

Spray coating uses compressed air to deposit fine droplets of the coating solution. This way, a thin, uniform coating layer can be produced over a large area. The main advantages of spray coating are scalability, rapid processing, and the ability to coat multiple layers autonomously. Typical parameters include a flow rate of 1 to 2 ml/min, nozzle height of 10 to 20 cm, air pressure between 1 and 3 bar and a head speed of 5 to 20 cm/s. These values are commonly used in air spray setups and fall within the ranges seen in experimental literature [57], [58].

The main advantages of spray coating are the scalability, rapid processing and the multitude of applications for this technique. A study has shown that spray-coated Pt-infused KB can exhibit high ECSA, making it a suitable technique for PEMFC applications[58]. On the other hand, spray coating is less precise than, for example, jetting. Overspray and material loss are more common. Moreover, less precise control over the atomising can affect coating thickness and uniformity [59], [60].

2.3.4 Ultrasonic spray coating

Ultrasonic spray coating is an advanced coating technique used to produce low Pt MEAs. This technique offers precision, better control, and a smaller drop distribution compared to other spray coating applications. Because of these distinct advantages, ultrasonic spray coating is increasingly replacing traditional air spray in various industrial and Research and Development (R&D) applications such as fuel cell manufacturing, photo resistor coating and solar cell production [61].

In this process, the liquid precursor undergoes ultrasonication. This way the liquid gets atomised before compressed air guides the Pt particles to the sample. Nozzle speed and height together with temperature, air pressure and flow rate define the coating quality. Using the software, these parameters can be optimised. To ensure a homogeneous coating, a horizontal and vertical pattern is repeated until the desired Pt loading is achieved [61], [62].

Commonly reported parameters include flow rates between 0.1 and 1.0 ml/min, spray head heights between 3 and 10 cm and substrate temperatures around 50 to 90 °C, which helps with faster solvent evaporation. Ultrasonic spray coating systems work best with inks that have a viscosity of 1 to 10 mPa·s and moderate surface tension between 25 and 35 mN/m. With these values, fine atomisation can be achieved without clogging or mist dispersion. Figure 11 shows results when optimising the header height.

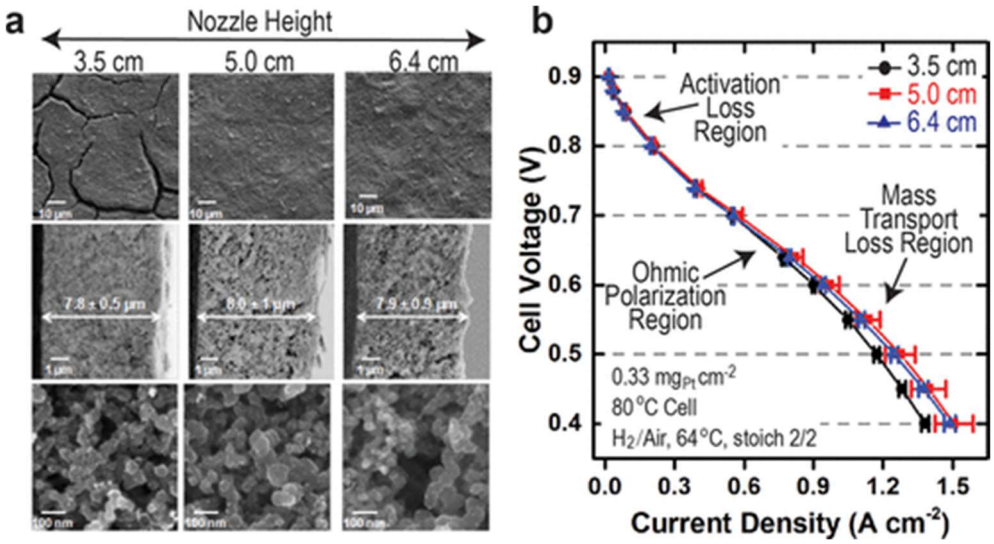

Figure 11: (a) SEM pictures of a directly coated membrane using an ultrasonic spray coater with different head heights. The top shows the exterior, the middle shows the cross-section and the bottom shows the interior. (b) Polarisation curves of MEAs [63]

Compared to air spray coating, ultrasonic spray coating suppresses the coffee ring effect via atomisation. Here, better dispersion of the fine droplets decreases the drying time which minimises internal flow and migration of the Pt particles. With the suppression of the coffee ring, the uniformity of the catalyst particle distribution improves while reducing agglomeration [56], [62]. However, the high cost and low throughput of the ultrasonic spray system are the main disadvantages compared to other techniques. The porosity of the catalyst layer is a benefit for surface active catalysts like Pt hindering mass transport [64], [65], [66].

With the increasing evolution of the fuel cell market, ultrasonic spray coating is becoming more important in laboratories. With all technologies, advanced modelling and simulation with AI can help predict coating thickness and improve other parameters that impact coating quality. According to Turtayeva *et al.*, heterogeneous thickness electrodes have an overall lower performance than homogeneous coatings in PEMFC testing, which is a key advantage of ultrasonic spray coating over other techniques, making it more desirable [62]

The different spray coating techniques each offer different strengths and weaknesses. Hand spray coating provides the most flexibility but lacks reproducibility which is important in this application. Air spray coating is fast, scalable and easy to implement but can have more material waste. Ultrasonic spray coating offers the most control over the uniformity but has the highest cost.

2.3.5 Conventional methods

In addition to the advanced deposition techniques investigated, several conventional electrode coating methods were researched briefly. These include brushing, dip/drop casting, blading, screen printing and manual hand spray coating.

Among the conventional methods, hand spray coating was included for its practical relevance during early-stage ink screening and R&D. This technique is manually operated and involves applying the ink to the substrate using a handheld sprayer. While it offers fast prototyping, which is useful for iterative development, it is highly dependant on operator consistency. Variables such as hand speed, angle, and

distance lead to inconsistencies between operators and coatings. As such, hand spray coating is used as a benchmark for the other deposition techniques.

Another widely known conventional method is screen printing, which is commonly used for SOEC electrode fabrication. It involves pressing a thick, high-viscosity ink through a mesh onto a substrate, followed by drying and sintering. This method is inexpensive and compatible with ceramic materials. However, as this method offers limited control over microstructure and thickness, the print can vary in quality. Therefore, this complementary part of the thesis investigates the feasibility of using jetting or spray coating deposition methods which could provide more control over the final print quality and reproducibility.

3 Materials and Methods

3.1 Materials

The catalyst powder consisted of 50 wt% Pt in Ketjenblack® (Pt/C) EC-300K, obtained from Fuel Cell Store (USA). KB was chosen over Vulcan XC-72 due to its high surface area and excellent electrical conductivity improving the catalyst performance [12].

The ionomer used to promote proper proton conductivity within the catalyst layer was Nafion® D2020CS, a 20% ionomer dispersion in ethanol purchased from Ion Power, USA. Nafion® was selected for well-documented performance in PEMFC application [17]. The amount of Nafion® was optimised to achieve sufficient TPBs without compromising gas diffusion. All materials were used as received without further purification or modification.

The ink solvent was prepared using 2-propanol (≥99.5% purity, Sigma-Aldrich, Germany; catalog no. I9516) and Milli-Q water. A volumetric ratio of 80:20, 2-propanol to water, was used to balance solvent evaporation rate and ink stability. The high ratio of 2-propanol helped to promote faster drying during the coating processes, reducing the risk of inhomogeneous coating due to poor solvent drying.

The substrates used for catalyst deposition were 3D-printed porous metal meshes that were in-house produced. The meshes had a fiber thickness of 0.4 mm and a square length of 25 mm and were used for fuel cell performance tests. This measurement is standard for this fuel cell application.

3.2 Equipment and instrumentation

Several coating systems and supporting equipment were utilised during this thesis. Jetting deposition was performed using a PICO Pµlse System from Nordson Ltd., USA. The technique was chosen based on the digitally controlled drop-on-demand ink application. This system allowed for precise optimisation of droplet size, jetting frequency and substrate distance to achieve a uniform layer deposition.

Ultrasonic spray coating was carried out with a Prism 500 Ultra Coat system from Ultrasonic Systems Inc., USA. The device used a high-frequency ultrasonicator to atomise the ink into a fine mist, producing a uniform thin film while reducing clogging, which is common for nozzle-based systems.

Air spray coating was performed using a Preeflow Eco-Spray system from ViscoTec, Germany. Hand spray coating was performed using an Evolution CR-plus manual spray gun from Harder & Steenbeck, Germany. These techniques served as a reference coating for their fast and reliable deposition. They were also both in-house optimised before coating.

Supporting equipment included a heating plate, used to preheat the substrates to 80 °C during coating, improving the evaporation rates. A precision mass balance with a precision of 0.1 mg to measure the catalyst loadings before and after deposition. An ultrasonic bath was used to homogenise the catalyst ink prior to application, minimising possible clogging of the nozzle.

The rheological properties were characterised using a HAAKE MARS rheometer from Thermo Fischer Scientific, USA. The shelf-life and the stability of the catalyst suspension were analysed using a

Turbiscan LAB Stability Analyser from Microtrac MRB, USA. The device uses Static Multiple Light Scattering (SMLS) to monitor possible particle migration and aggregation over time. Each sample was scanned over a time span of two to 18 hours, and the resulting backscattering profiles were used to calculate the Turbiscan Stability Index (TSI). The TSI quantifies the extent of destabilisation, with values under 0.5 indicating good stability. Particle size distribution analysis of the ink was measured using a Partica mini from Horiba Scientific, Japan. Microstructure and elemental distribution of the prepared coatings were analysed via desktop SEM, coupled with EDX (ThermoFisher scientific Phenom PRO G6).

To automate the coating process of the jetter, a short Python script was written which generated a repeated serpentine pattern for the mesh. The script processes a base G-code file by isolating the repeated body from the initialisation segment and programmatically repeats the body section a given number of times. The final code, used to streamline the code generation, can be found in Figure 34 of the Appendix. This semi-automated approach significantly reduced manual editing time while removing any mistakes in the body.

3.3 Ink preparation

To create a homogeneous and stable catalyst ink for electrode fabrication, a 2-propanol/water-based suspension was prepared. The formulation was optimised for consistency, dispersion stability, longer shelf-life and compatibility with the different coating techniques. First, a catalyst ink with a concentration of 1.50 mg/ml Pt/C was prepared by dispersing the Pt/C powder into a solvent mixture consisting of 80 vol% 2-propanol and 20 vol% deionised water. Afterwards, 1.50 mg/ml Nafion® solution was added to the mixture under continuous stirring.

The mixture was ultrasonicated for 10 minutes using an ultrasonic bath to ensure complete dispersion of the catalyst particles while preventing agglomeration. The resulting suspension was stored at room temperature in a sealed container where it remained stable for at least a week. The suspension was suitable for each coating technique.

Prior to each coating process, the substrates were preheated on a hotplate to 80 °C to promote adhesion and speed up evaporation. The suspension was ultrasonicated for at least 10 minutes before each coating session to mitigate any agglomeration that happened during storage and improve uniformity. Specific pre-treatment adjustments were made for each coating technique and are described in detail in the next section.

3.4 Coating techniques and parameters

3.4.1 Jetting

Jetting deposition was performed using a PICO Pµlse System, shown in Figure 12. In this setup, piezoelectric pulses generate individual drops through a 100 µm nozzle. This allows for a precise pattern to be followed with minimal material loss. The system was chosen for this application due to the high level of control over the deposition parameters which is important for coating porous substrates such as the 3D-printed meshes.

Figure 12: Experimental setup of the drop-on-demand jetting system

The coating sequence was designed to follow the fiber pattern of the meshes in both the horizontal and vertical directions. Due to the small droplet size, each drop fully evaporated before the next one got deposited, which prevented excessive wetting or pooling. The number of passes required to achieve the desired catalyst loading was determined by measuring the area and the mass.

The key operational parameters for the coating procedure were the following. The substrate temperature was maintained at 80 °C, while the nozzle temperature was set at 60 °C. This was done to enhance the droplet evaporation. The pulse time was configured at 0.275 ms, combined with a jetting frequency of 333.33 Hz. A substrate-to-nozzle height of 3cm was maintained during the coating process. The speed of the head was 200 cm/min, and the reservoir pressure was set at 0.5 bar. These parameters were chosen for the final coating after iterative optimisation. Optimisation trials were first conducted on glass substrates, to visually assess the deposition quality.

3.4.2 Air spray coating

Air spray coating was performed using an Eco-Spray system, shown in Figure 13. This is a conventional technique for this application. In this process, compressed air at the nozzle directs the ink to the sample, allowing for relatively faster coating.

Figure 13: Coating setup for the air spray coating samples

The key operational parameters were optimised as follows: a nozzle-to-substrate distance of 10 cm was maintained, and the system pressure was 1.0 bar. The movement speed of the spray head across the substrate was kept at 10 cm/s and the ink flow rate was 1.0 ml/min. The substrate was heated to 80 °C during coating to obtain faster solvent evaporation. Due to the high air pressure and the low weight of the 3D-coated meshes, the substrate was secured with double-sided tape to prevent it from being displaced. Additionally, because of the relatively high ink volume dispensed from the air spray system, practical challenges were encountered. The directional change of the spray header at the end of each pass occurred further from the sample than desired. This led to increased material losses.

3.4.3 Hand spray coating

Hand spray coating was performed using an Evolution CR-plus manual spray gun. The method used compressed air to atomise the ink, with manual control over the spraying motion and deposition pattern. During the coating procedures, a distance of approximately 10 cm between the nozzle and the substrate was maintained, and the system was operated at 1 bar of air pressure. This method was the only one that did not heat the substrate to 80 °C during the coating, which slowed the evaporation speed. Figure 14 shows the hand spray coater.

Figure 14: Manual hand spray coater

3.4.4 Ultrasonic spray coating

Ultrasonic spray coating was performed using a Prism 500 Ultra Coat system, shown in Figure 15. This method utilises a high-frequency ultrasonicator to generate vibrations. The ultrasonic head atomises the ink into a fine and uniform aerosol. For all experiments, the nozzle-to-substrate distance was maintained at approximately 10 cm, and the substrate was heated to 80 °C to accelerate solvent evaporation during deposition. The arm speed was 1 cm/s, and the flow rate was 0.25 ml/min.

Figure 15: Ultrasonic spray coater head used for ultrasonic spray coating samples

To achieve a uniform coating, ultrasonic spray coating parameters such as nozzle height, flow rate, and substrate temperature were optimised through a trial-and-error approach. These trial coatings were first conducted on flat paper substrates to validate the spray pattern before transferring to the 3D-printed meshes.

3.4.5 Coating parameter optimisation

To optimise the coating protocol for jetting and ultrasonic spray coating, a series of parameter studies were conducted following a One Factor At a Time (OFAT) approach. In this method, only one independent process parameter was varied at a time while other variables were held constant. This way, the individual effect of each parameter on the coating quality could be assessed.

For jetting, parameters such as the height between substrate and nozzle, substrate temperature, pulse time, frequency and arm movement speed were investigated. The primary goals were the improvement of the droplet deposition and formation quality. By visually assessing the droplet size uniformity, absence of satellite drops and spacing between the drops with the use of macro photographs, the deposition and formation could be optimised. The specific parameters that were investigated for jetting are summarised in Table 1.

Table 1: Parameters of OFAT method used to optimise the jetter

Parameter	Range tested
Nozzle to substrate height (cm)	2 - 5 - 10
Substrate temperature (°C)	40 - 60 - 80
Pulse time (ms)	0.275 - 0.600 - 1.000
Droplet frequency (ms)	20 - 25 - 40
Arm movement speed (mm/s)	1000 - 2000 - 5000

Each tested parameter and range are listed in Table 1, showing the low, medium and high values respectively. These values were used in trial coatings to visually assess coverage uniformity and drying behaviour. Figure 16 illustrates the visual improvement between a non-optimised parameter set (A), a sample during the optimisation process (b) and the final optimised deposition protocol (c).

Figure 16: Visual comparison of the optimisation process of the jetter. (a) Starting parameters results in non-uniform coverage and drying artefacts. (b) improvement but still a high agglomeration and waste visible. (c) Optimised parameters

For ultrasonic spray coating, parameters such as flow rate, the height between substrate and nozzle, substrate temperature and arm movement speed were studied. The focus was on the uniformity of the deposited catalyst layer, assessed through visual inspection. The specific parameters that were investigated for ultrasonic spray coating are summarised in Table 2.

Table 2: Parameters of OFAT method used to optimise the ultrasonic spray coater

Parameter	Range tested
Nozzle to substrate height (cm)	30 – 50 - 70
Substrate temperature (°C)	40- 60 - 80
Flow rate (ml/min)	0.1- 0.25 - 0.5
Arm movement speed (cm/s)	1- 5 - 10

A similar OFAT strategy was applied to optimise the ultrasonic spray coater, using low, medium and high values for the ranges shown in Table 2. Visual comparison of the resulting coatings are presented in Figure 17.

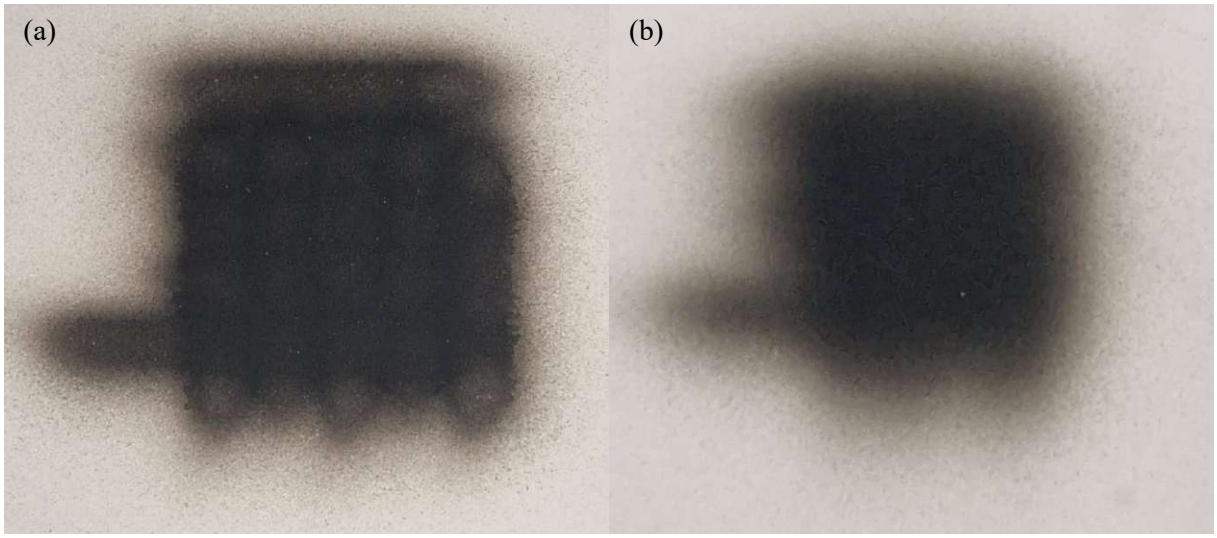

Figure 17: Visual comparisons of ultrasonic spray-coated layers. (a) Starting parameters result in non-uniform coverage and drying artefacts. (b) Optimised parameters leading to homogeneous and uniform catalyst layer

Data collected during the OFAT experiments were used for response curves that show coating quality as a function of each varied parameter. In addition, photographs taken during optimisation were used to illustrate the effect of parameter changes. While a proper Design Of Experiments (DOE) approach would offer a more rigorous statistical analysis and insight into the interaction between variables, it was not feasible due to time constraints. Therefore, the results can only analyse the individual influence of each factor under the fixed conditions of the others.

3.5 Solid Oxide Electrolysis Cell preparation

Slurries were prepared by firstly mixing organic binders, namely ethyl cellulose (ACROS Organics) with ethanol (96 %, Merck), polyvinyl pyrrolidone (Janssen Chimika) and poly vinyl butyral (Acros), followed by the addition of $Ce_{0.9}Gd_{0.1}O_2$ (GDC) and $Ca_{0.4}Sr_{0.4}Co_{0.12}O_3$ (CSCO) powders (both obtained from Marion Technologies). The mixture was stirred until it was homogeneous. Each slurry contained a powder loading of 10 wt% with a ratio of GDC: CSCO of 1:1. Prior to mixing the powder was sieved to a particle size of 40 µm to ensure no clogging of the nozzles. To coat homogenous and uniform electrode layers to the desired thickness, each coating suspension and the coating parameters were

optimised. One of the key parameters of the suspension is the stability. To control the suspension stability , SMLS and particle size distribution were measured. GDC button substrates were deposited by the prepared inks, dried in the air, and subsequently heat treated in the air at 520 °C for 2 hours and at 900 °C for 4 hours before cooling down to room temperature. Heating rates were set at 60 °C/h and cooling rates at 120 °C/h.

3.6 Characterisation techniques

3.6.1 Ink Stability Analysis

Ensuring the stability of the catalyst ink suspension was important for achieving reproducible and high-quality coatings. For this, a combination of SMLS, particle size analysis and rheological measurements were used to characterise the stability and flow behaviour of the ink.

SMLS measurements were conducted to monitor transmission and backscattering through the sample over time, detecting possible sedimentation or creaming phenomena. Each ink batch was monitored continuously for six hours, after which the software analysed the stability behaviour and shelf-life. In addition to SMLS, particle size distributions were measured to evaluate the possible agglomeration of KB particles in the suspension. Agglomeration of particles inside the ink could negatively affect spray performance, coating uniformity and nozzle clogging. Finally, the rheological properties of the ink were characterised. Viscosity measurements were used to determine the flow behaviour of the inks under deposition conditions.

3.6.2 Morphological characterisation

Characterising the morphology of the catalyst layer was important for evaluating the coating quality and the uniformity of the platinum distribution on the 3D-printed mesh. To properly assess the morphological structure, a combination of Optical Microscopy, SEM and EDS was used.

Optical microscopy served as a preliminary assessment of the coating quality over large areas. Surface images were taken to identify possible macroscopic defects and non-uniform patterns. Subsequently, SEM analysis was performed to investigate the surface uniformity, coating thickness and porosity of the catalyst layer. Prior to the SEM imaging, the samples were embedded in a polymer resin to ensure structural integrity during sectioning. Afterwards, cross-section SEM micrography was taken and allowed for the evaluation of the thickness of the coating, internal structure and adhesion of the catalyst layer to the porous metallic substrate. In addition, EDS was used to perform elemental mapping. This was used to confirm the platinum distribution across the coated layer and to identify possible inhomogeneities. For the SOEC samples, SEM and EDS images were obtained from both the top-surface and cross sections of the GDC-CSCO electrode, coated on the GDC substrate. The samples were imaged as received. The cross-sections of the samples were obtained by fracturing the coated electrode and substrate vertically without polishing.

3.6.3 Fuel cell performance testing

To properly evaluate the operational performance of the coated electrodes under *in-situ* PEMFC conditions, fuel cell performance tests were performed. The catalyst-coated meshes were assembled as the anode in a test cell at a controlled temperature and gas flow rate. The MEA was prepared by stacking

a Nafion® ionomer membrane between the catalyst-coated mesh and a 0.75 mg_{Pt}/cm^2 coated carbon paper. The assembly was then placed in an oven and heated to 110 °C under constant weight to promote bonding.

Polarisation measurements were conducted to evaluate the performance of the PEMFC under ambient laboratory conditions. These curves provided insight into common losses, such as activation losses, ohmic resistance and mass transport limitations. During the measurements, the cell operated at room temperature without active temperature control. Hydrogen and oxygen were supplied to the anode and cathode, respectively, at flow rates of 0.2 L/min. The oxygen stream was humidified using a water bubbler at room temperature, while hydrogen was supplied dry. The fuel cell operated at ambient pressure, with no backpressure applied. A potentiostat was used to perform linear sweep voltammetry, scanning from the Open-Circuit Potential (OCP) to 800 mV below OCP at a scan rate of 10 mV/s. Prior to measurements, the cell was allowed to stabilize under these conditions to ensure consistent performance.

3.6.4 Electrochemical impedance spectroscopy

Electrochemical impedance spectroscopy measurements of prepared symmetrical cells were carried out by NORECS AS, using an in-house set-up, based on a commercial probostat reactor. Flowrates of purging gasses were controlled via mass flow controllers (Bronkhorst High-Tech B.V., model El-flow metal sealed). Measurements were done in pure N_2 (Air products, BIP grade, 99.9999% purity) or synthetic air (Air products, technical grade). Prior to measurement, Ag current collector layers were applied to coated electrodes on both sides via silver paste brushing (AG-I silver ink, Fuel cell materials) followed by drying at 150°C for 1 hour and annealing at 800°C on air for 1 hour, in order to remove organic parts of the ink.

3.7 Economic feasibility analysis

For comparing the economic feasibility of the different coating techniques, the Capital Expenditures (CAPEX) and Operational Expenditures (OPEX) of each technique was analysed based on, the coater pricing and material pricing as well as the experimental data obtained in this work. CAPEX was taken directly as the coating equipment cost in euros. OPEX was calculated from the mass of Pt used for a full coating of ca. 0.77 mg_{Pt}/cm^2, as the Pt cost has the highest impact on the total PEMFC manufacturing cost. From the Pt cost per coating, the other results were calculated. Equation 3.1 shows the calculation of the OPEX cost per coating divided by the cell performance.

$$\frac{\text{OPEX}}{\text{Performance}}\left(\frac{€}{W}\right) = \frac{\text{OPEX}\ (€)}{\text{Area}\ (cm^2) * \text{Max power density}\left(\frac{W}{cm^2}\right)} \tag{3.1}$$

This metric, expressed in €/W, reflects how the OPEX contributes to the max power density. For a direct comparison of material efficiency between the different techniques, the cost per coated area was calculated as shown in Equation 3.2.

$$\frac{\text{Cost}}{\text{Area}}\left(\frac{€}{\text{cm}^2}\right) = \frac{\text{OPEX (€)}}{\text{Area (cm}^2\text{)}} \tag{3.2}$$

Together, these metrics provide a consistent framework to compare the cost-effectiveness of each coating method concerning both material usage and performance.

4 Results and Discussion

4.1 Suspension optimisation

The quality and stability of the ink suspension were evaluated and optimised using three primary techniques: Turbiscan stability analysis, rheological profiling and particle size distribution. The optimisation process aimed to create a formulation with enhanced long-term colloidal stability, suitable viscosity for the coating techniques and compatibility with the different nozzles. Multiple ink formulations were prepared, with a focus on varying the solvent ratio (water to IPA), Nafion® ionomer content and Pt/C concentration.

4.1.1 Turbiscan stability analysis

The suspension stability was evaluated using the Turbiscan LAB analyser. This technique monitors light transmission and backscattering through the ink sample over time, enabling the calculation of the TSI. The TSI provides a quantitative measure of the destabilisation of the sample over time. Generally, values under 0.5 are considered stable and safe for coating processes. To improve the evaporation characteristics of the suspension, an increase in IPA concentration was tested, as shown in Figure 18.

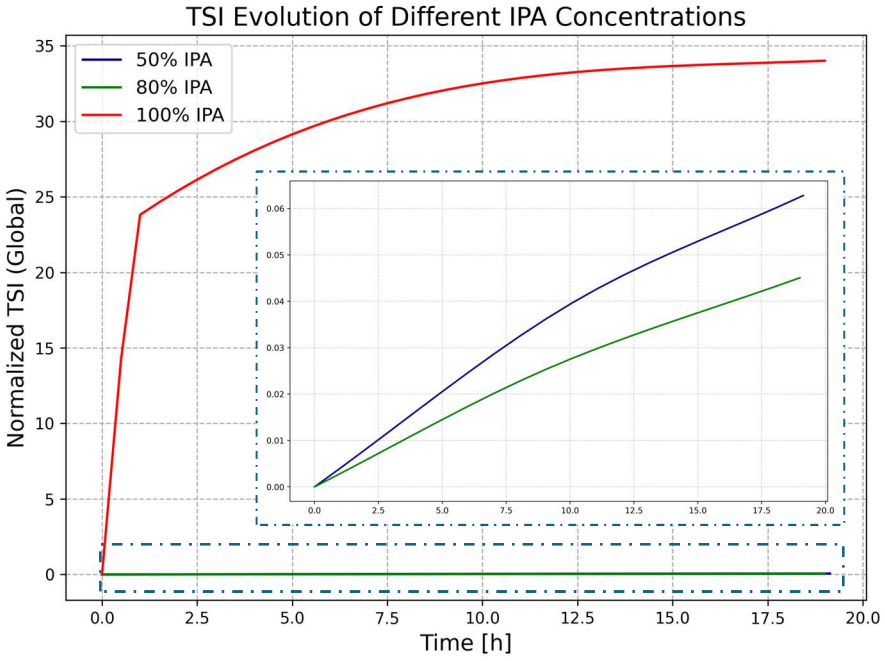

Figure 18: Impact of the TSI of suspensions with different IPA (50%, 80% and 100%) concentrations on the stability of the suspension over time. The inset figure is the zoomed-in TSI Evolution for the 50% and 80% IPA

Figure 18 shows that increasing IPA content from 50% to 80% improved drying behaviour while increasing the overall stability of the ink. Increasing the IPA concentration to 100%, however, shows a significant decrease in colloidal stability. Therefore, an 80% IPA-in-water mixture was selected as the optimised solvent ratio for the subsequent stage of ink optimisation. After optimising the solvent ratio,

the influence of varying the added amounts of Pt/C and Nafion® was examined. Figure 19 shows the TSI evolution for suspensions that have a changing IPA concentration, Pt/C concentration and the use of Nafion.

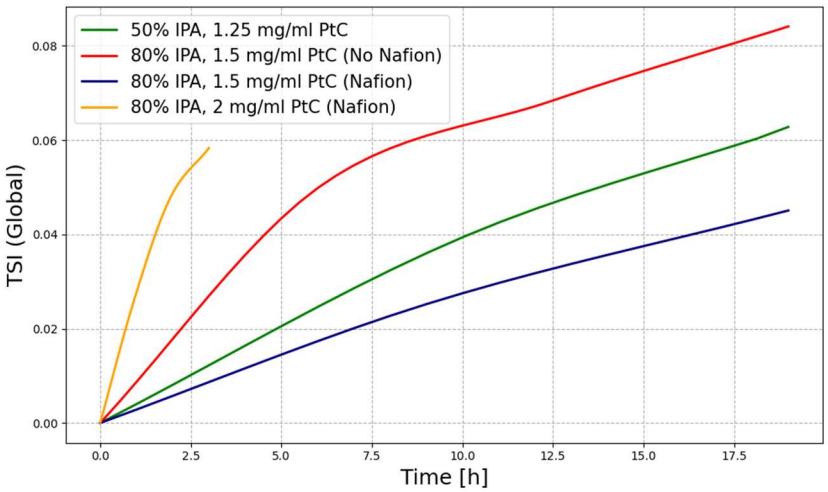

Figure 19: Comparison of different concentrations of IPA, Pt carbon black and Nafion on the stability of the suspension over time

The four suspensions were assessed. When increasing the Pt/C concentration above 1.50 mg/ml, the overall stability of the suspension decreased. Also, the absence of Nafion® led to increased sedimentation and thus a higher TSI. The ink formulation was finalised as, 80% IPA, medium Pt/C concentration (1.50 mg/ml), and Nafion® (1.50 mg/ml), providing the best balance between shelf life and evaporation speed.

4.1.2 Rheological measurement

A viscosity profile of the optimised Pt/C ink was measured, prior to being used in all the coating methods. The resulting viscosity and shear stress as a function of shear rate are presented in Figure 20.

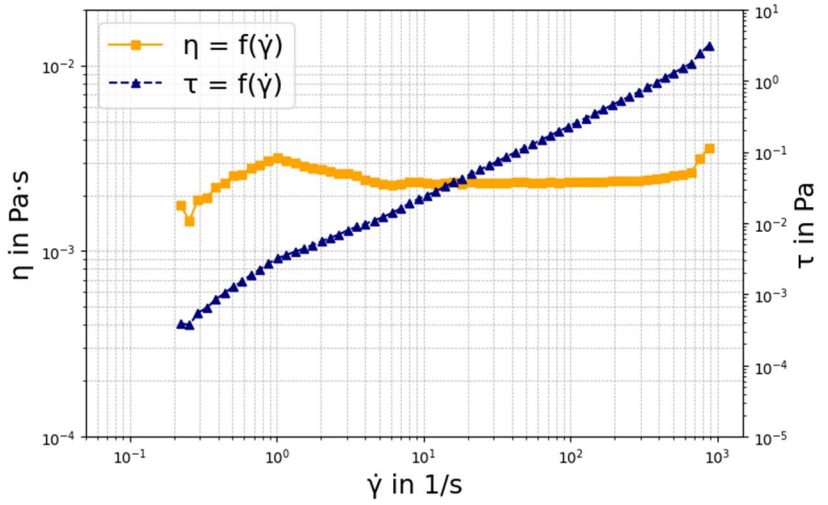

Figure 20: Logarithmic plot of the viscosity profile of optimised Pt/C ink used in all the coating methods

The results indicate that the ink exhibits near-Newtonian behaviour at moderate shear rates and a slight shear thinning trend at higher rates. The viscosity remained in the optimal range for the coating techniques and was approximately between 1 and 10 mPa·s, which was ideal for both jetting and ultrasonic spray coating. Jetting is optimal within a viscosity range between 1 and 20 mPa·s which facilitates stable droplet formation while minimising the risk of satellite droplets and nozzle clogging [67]. The ultrasonic spray coater, used in this work, utilises a viscosity range is between 1 and 100 mPa·s. Spray coating and hand spray coating still benefit from moderate viscosity to control film thickness, but are less sensitive to small changes in viscosity than the other two techniques.

4.1.3 Particle size distribution

To ensure no nozzle clogging, the Particle Size Distribution (PSD) was assessed. The jetting nozzle had the smallest nozzle diameter of 100 µm. The measured particle sizes, shown in Figure 35a in Appendix B, revealed that the Pt/C particles remained under 10 µm in diameter, with no significant agglomeration. This confirmed their suitability for all the coating methods and ensured no nozzle clogging.

Based on the combination of stability, viscosity and particle size assessment, the 80% IPA with 1.50 mg_{Pt}/cm^2 and Nafion® was selected as the final ink formulation. It demonstrated long-term dispersion stability, Newtonian flow characteristics and full compatibility with all coating techniques.

4.2 Morphological characterisation

With the suspension optimised, the morphological characteristics of the coated electrodes were assessed. The quality of the deposited electrode layers is crucial for evaluating the effectiveness of each deposition technique on the electrode behaviour and cell performance. For this reason, a combination of optical microscopy, SEM and EDS was employed. Each coating method was examined with the same optimised ink formulation, explained in Section 4.1. By using the same suspension, the coating uniformity, thickness and material distribution of each deposition technique are assessed.

4.2.1 Surface morphology

Initially, optical microscopy was used to evaluate the large-scale visual uniformity of the coatings. Although optical microscopy lacks the resolution required to detect microstructural features, it was effective as a rapid screening method for identifying macroscopic defects such as cracks, delamination, or incomplete coverage. All coating methods yielded visually uniform films, with no observable macroscopic defects, shown in Figure 36, Figure 37 and Figure 38 in the Appendix.

In addition to the quick screening, an optical microscope is also used to visualise the 3D-printed mesh structure before and after coating, which gives insight into the porous structure of the mesh and how the coating fills up that porous structure. The comparison in Figure 21 shows a clear reduction in the porosity and confirms that the coating successfully bonded on the porous structure.

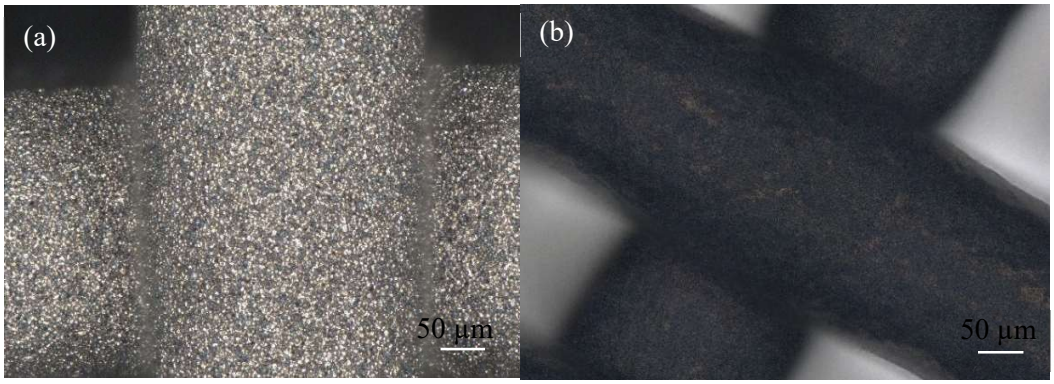

Figure 21: Top view optical images for (a) the before and (b) after 0.8 mg_{Pt}/cm^2 coated mesh

Figure 21 displays both the surface appearance of the uncoated and coated mesh at an optical magnification of 500x. No significant surface-level visual difference is detected across the different deposition methods.

4.2.2 Microscopical morphology

SEM imaging provided deeper insight into the coating uniformity and the layer morphology. SEM images were taken from both top-down and cross-sectional perspectives at magnification ranging from 100x to 5000x. Coating experiments with Pt/C inks prepared without Nafion® revealed poor adhesion to the substrate, resulting in progressive delamination of the catalyst layer over time. This is shown in Figure 22, which shows the cross-section of a coated electrode without the use of Nafion®.

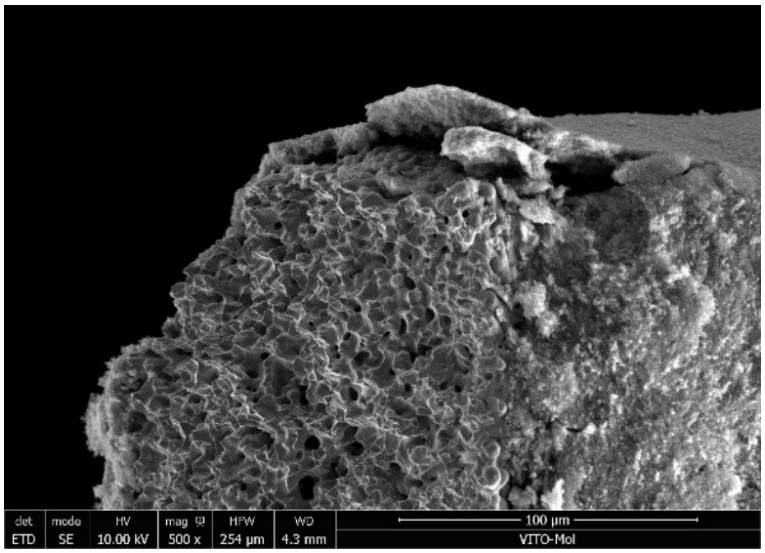

Figure 22: Cross section of a Pt/C coating without Nafion® deposited on the 3D printed mesh

As seen in Figure 22, the coating has delaminated from the mesh substrate which indicates poor adhesion to the mesh. Strong adhesion at the coating substrate interface, together with the higher long-term stability of the coating suspension and its ion conductivity properties, makes the use of Nafion® both as an ionomer and binder vital for the best coating results. Furthermore, Nafion® ensures mass transport and access to the Pt catalyst particles at TPB, making it indispensable for PEMFCs.

To assess the internal morphology and the coating uniformity of the thickness of the catalyst layer, cross-sectional SEM imaging was conducted at 120x magnification. Figure 23 shows the full cross sections of a fiber, coated with Pt/C catalyst ink via jetting and ultrasonic spray coating respectively.

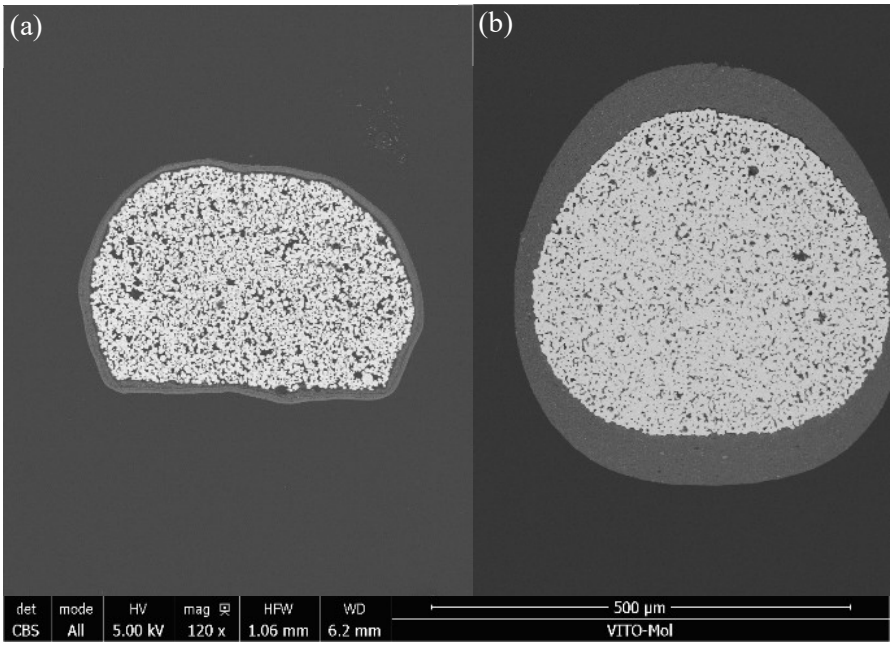

Figure 23: Cross-section at 120x magnification of a fiber, coated with Pt/C catalyst with (a) 0.75 mg_{Pt}/cm^2 loading via jetting and (b) 1.50 mg_{Pt}/cm^2 via ultrasonic spray coating

The cross-sectional SEM micrograph of the jetting sample (Figure 23a) shows a uniform and symmetric catalyst layer that conforms closely to the fiber. The even distribution is likely due to the controlled, drop-on-demand deposition combined with optimised drying conditions, which prevented pooling or uneven accumulation. In contrast, the ultrasonic spray-coated sample (Figure 23b) exhibits a distinctly, asymmetric, oval-shaped layer, with significantly thicker deposition on the exposed sides during coating. This non-uniformity is likely the result of directional coating combined with rapid solvent evaporation. Next, the cross-section of the four coating techniques is measured in the SEM. Figure 39 in the Appendix shows the 500x magnification of each deposition technique. Figure 24 shows the 2500x magnification of the four deposition techniques.

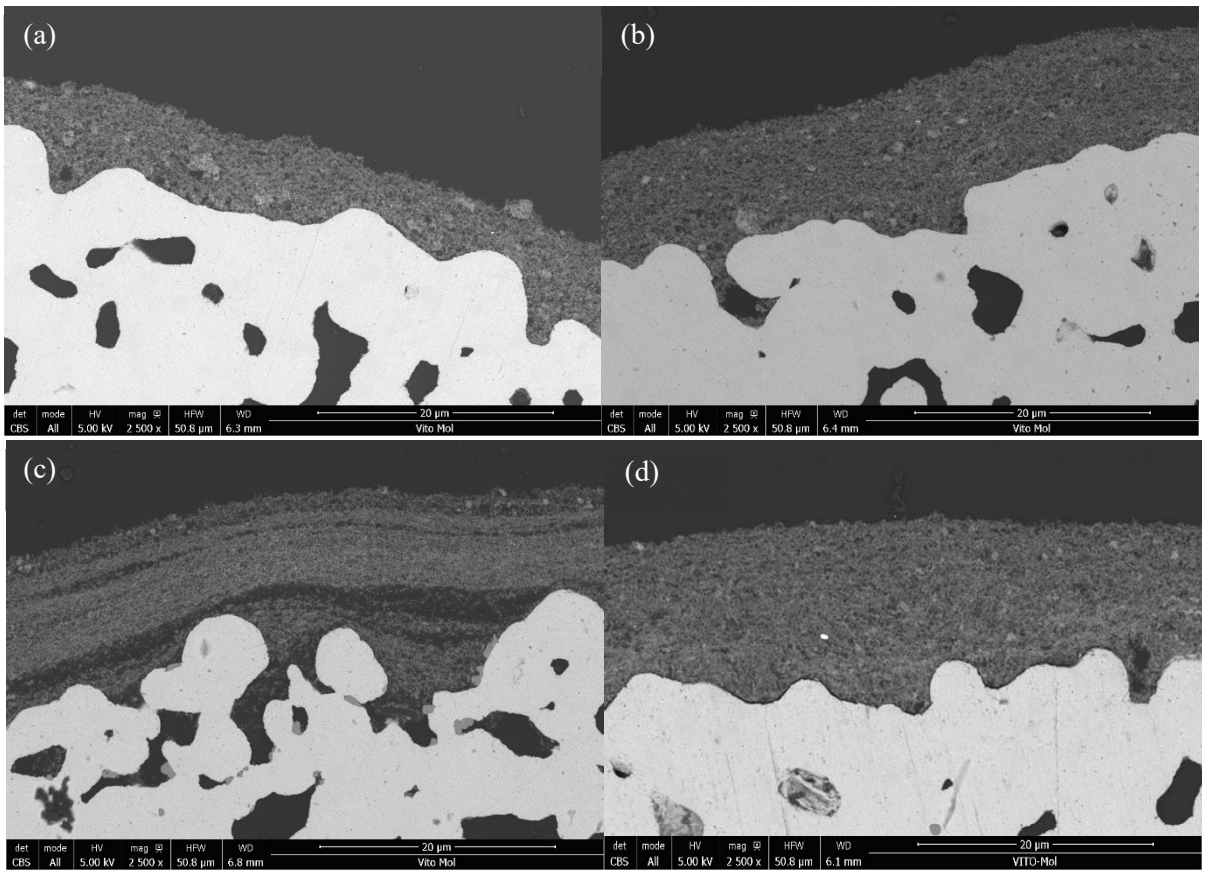

Figure 24: Cross-sectional SEM micrograph of 3D printed meshes, coated with each technique: (a) air spray coating, (b) hand spray coating, (c) jetting and (d) ultrasonic spray coating. All images were captured at 2500x at HV of 5 kV and a working range of 6.3-6.8 mm

The cross-sectional micrograph in Figure 24 shows clear differences in morphology and quality of each coating produced by the four techniques. At first inspection, air spray coating (Figure 24a) and jetting (Figure 24c) produce highly porous and structurally irregular layers, respectively, whereas hand spray coating (Figure 24b) and ultrasonic spray coating (Figure 24d) result in denser and more uniform films.

The air spray technique (Figure 24a) produced a significantly more porous structure. The coating exhibits large, irregular spaces throughout the layer, indicating less homogeneity and less efficient deposition. Furthermore, the layer is visibly inconsistent in thickness, and there is a small space at the interface, indicating minor detachment. These observations suggest inadequate spray control during deposition, which possibly leads to higher surface wetting and more inconsistencies in the final layer. Compared to air spray, the hand spray method (Figure 24b) demonstrated an improvement in both uniformity and porosity. The voids are smaller but more evenly distributed, while the overall coating has better thickness control. The improved performance is likely due to the smaller coating flow rate, which improves the drying time of the coating.

The jetting technique (Figure 24c) yields a highly porous structure with significant morphological irregularities. The pores form channelled voids, indicating unstable deposition. The coating thickness varies considerably, while the coating seeped deep into the mesh. Furthermore, the interface quality is poor with visible detachment zones and minimal bonding to the surface. Despite the precision technique, the poor result indicated challenges in maintaining droplet consistency during jetting.

Upon closer inspection, the difficulty seems to arise at the start of some coating cycles. At that stage, the ink appears to be visually lighter, indicating that mainly solvent is being deposited and carbon

particles are blocked. This likely indicates that there is a pressure build-up in the nozzle. The low ink pressure of 0.5 bar does not clear this blockage, allowing only the liquid phase to exit. As this phenomenon happens rarely and stays for an uncertain time, there is no exact moment to know when the carbon particles resume normal deposition. One approach to mitigate this problem is to increase the nozzle pressure before each coating cycle. This effect impacts the morphology and is related to a device-specific startup limitation pointing to the benefits of the non-clogging device design utilising ultrasonic vibration and atomisation.

The ultrasonic spray coating (Figure 24d) delivers the most desirable morphology. The layer is dense, has minimal voids and has a consistent thickness at 2500x magnification. The interface shows a small space between the coating and substrate, indicating lower adhesion. The morphological result indicates that the fine atomisation promoted the controlled deposition and improved solvent evaporation causing this technique to outperform the others in terms of coating quality.

4.3 Elemental composition

4.3.1 Platinum distribution

To complement the morphological analysis conducted via SEM, EDS was performed to investigate the elemental distribution for each coating technique. Figure 25 displays the EDS maps of the four deposition techniques at 2500x magnification, with Pt represented in magenta.

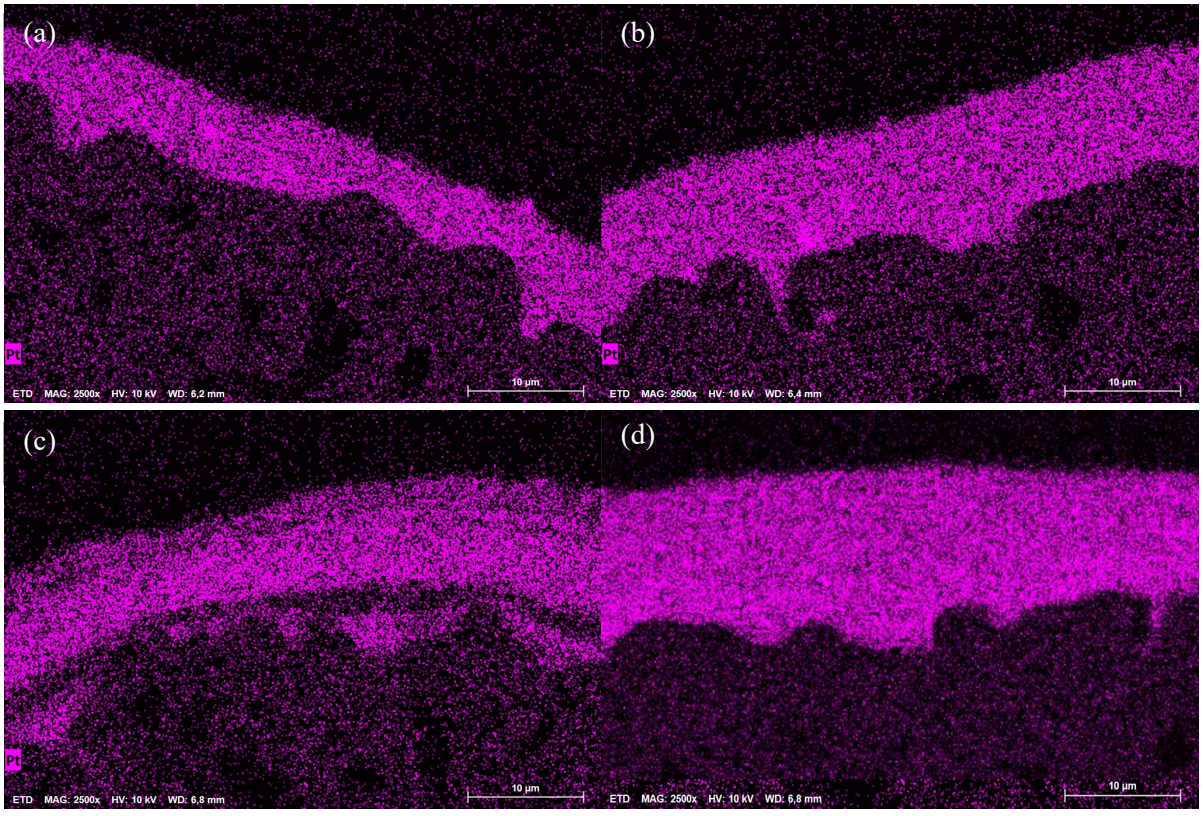

Figure 25: EDS mapping (Pt in magenta) of coatings produced using the four different techniques: (a) air spray coating, (b) hand spray coating, (c) jetting and (d) ultrasonic spray coating. Images were taken at 2500x magnification

In the EDS mapping for air spray coating (a), Pt appeared dispersed unevenly, with a combination of larger clusters and areas that lack a complete signal. This confirms that the uneven distribution correlates with the high porosity observed in the SEM image. The hand spray coating (b) has a better dispersion of Pt particles compared to air spray, but agglomeration and voids are still visible. The coating is thicker and more connected, but inconsistent density zones remain visible showing that this technique and air spray coating both lack the fine atomisation needed for uniform coatings.

The EDS image of the jetting technique (c) confirms the disordered distribution of Pt. The coating seeped deep in the substrate, and signal intensity fluctuated across the layer, showing Pt-rich regions with irregular voids, confirmed by the SEM image. This confirms possible fluctuations between the drops during coating, which impacted the overall coating result. Finally, the ultrasonic spray coating (d) delivers a dense and continuous Pt signal, showing an evenly distributed coating layer. The coating is uniform in both horizontal and vertical directions, with a consistent intensity and thickness. The fine atomisation helped with minimising the Pt-clusters and major voids.

4.4 Fuel cell performance evaluation

4.4.1 Comparison of medium-loading coatings

Polarisation curves were recorded to evaluate the PEMFC performance of each coated electrode. First, a comparison is made between the three most prominent coating methods. Hand spray coating is not a viable method for producing medium-loading samples as it is not scalable and has too much operator variation. The polarisation measurements were performed under ambient conditions (20 °C). The results provide insight into how each deposition technique impacts the catalyst layer performance. Figure 26 shows the voltage (V) as a function of the current density for the three main coating techniques: ultrasonic spray coating, air spray coating and jetting, all with a medium loading of 0.75 mg_{Pt}/cm^2.

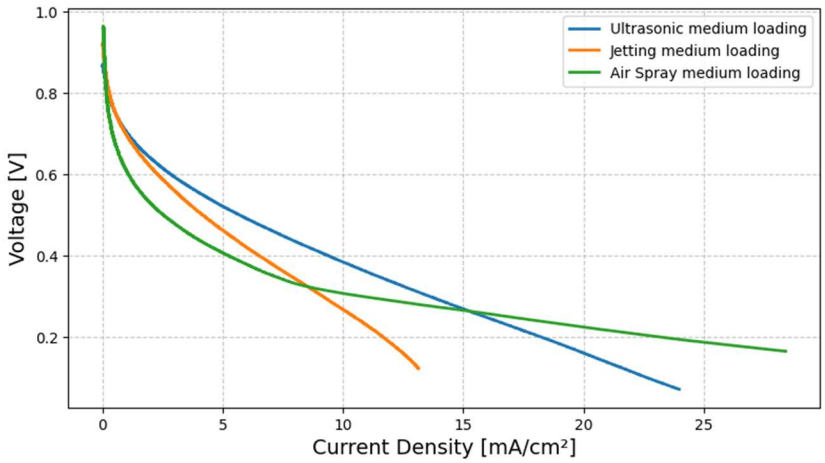

Figure 26: Comparison of voltage curves for ultrasonic spray coating, air spray coating and jetting deposition techniques for a medium loading of 0.75mg_{Pt}/cm^2

In the activation area (0-5 mA/cm^2), both ultrasonic spray deposition and jetting exhibit the best performance, which suggests a lower activation loss. The improved performance can be attributed to less agglomeration of Pt/C and better contact between the Pt/C particles and the ionomer, which

improves the ECSA. This can be corroborated by the EDS micrograph (Figure 25), which shows well-dispersed catalyst particles for ultrasonic spray coating and minimal agglomeration for both ultrasonic and jetting catalyst layers. In contrast, air spray coating demonstrates a significant voltage drop in this region, indicating higher activation losses. This is likely due to more catalyst agglomeration as there are larger Pt clusters visible.

In the medium current density region (5-10 mA/cm²), which corresponds to the ohmic loss region, jetting begins to underperform compared to ultrasonic spray coating. The non-uniform layer from jetting (Figure 24) results in greater internal resistance and thus, less efficient electron pathways, leading to an increase in ohmic losses. This non-uniform coating is evident in the SEM cross-section micrographs (Figure 24), which show the void formation.

As the current density increases further beyond 10 mA/cm², which corresponds to the mass transport limited region, air spray coating outperforms both jetting and ultrasonic spray coating. This is attributed to the more porous catalyst structures (Figure 24), which improve gas and ion diffusion and reduce the overall concentration polarisation. The SEM analysis of air spray coating shows a less compact and more open microstructure. Figure 27 shows the corresponding power density as a function of current density for medium-loading electrodes.

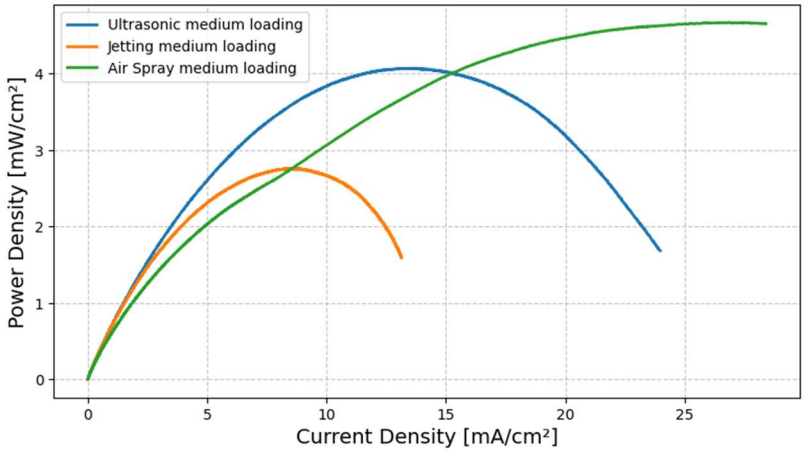

Figure 27: Comparison of power density curves as a function of the current density for ultrasonic spray coating, air spray coating and jetting for a medium loading sample of 0.75 mg_{Pt}/cm^2

The ultrasonic deposition method demonstrates the highest peak power density at a lower current density, reaching 4.07 mW/cm² at a current density of 13.74 mA/cm². This shows the balance between a relatively low activation loss and manageable ohmic losses. However, at higher current densities, the performance declines due to increasing mass transport limitations and internal resistance, causing a decline over 15 mA/cm²

The jetting method peaks lower, with a peak power density of 2.67 mW/cm² at 10.03 mA/cm² and then drops off rapidly. This indicates that the catalyst layer formed by jetting is less uniform or less integrated with the incomer, leading to both a lower amount of triple phase boundaries and an earlier onset of mass transport limitations.

In contrast, the air spray method shows a steady increase in power density, achieving the highest maximum power density value of 4.67 mW/cm² at a current density of 26.85 mA/cm². At lower current densities, a higher activation loss is visible. When increasing the load, the electrode maintains its

performance more effectively under increasing load. This suggests that the catalyst layer is more porous, allowing for superior mass transport at elevated currents.

4.4.2 Comparison between medium- and high-loading coatings

To evaluate the impact of catalyst loading on the fuel cell performance, voltage and power density curves as a function of the current density were compared. Figure 28 shows the voltage as a function of the current density for medium (0.75 mg_{Pt}/cm^2) and high (1.50 mg_{Pt}/cm^2) loadings.

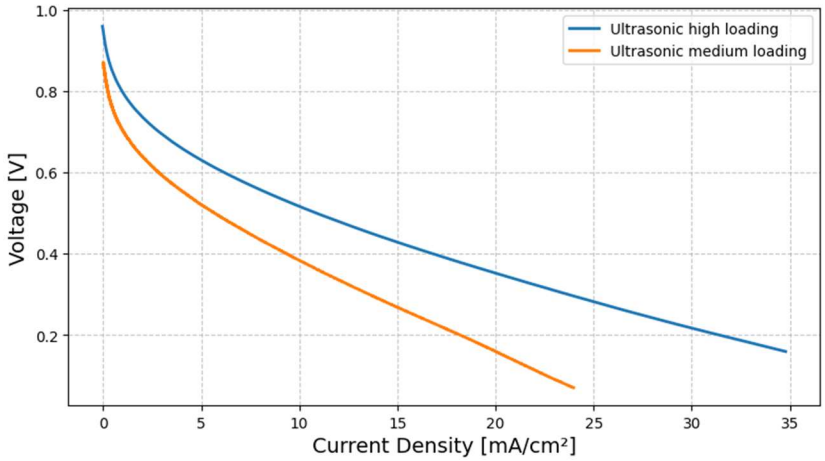

Figure 28: Comparison of voltage curves for ultrasonic spray coating with medium loading (0.75 mg_{Pt}/cm^2) and ultrasonic spray coating with high loading (1.50 mg_{Pt}/cm^2)

Across the whole current density range, the high catalyst loading cell consistently outperforms the medium loading cell. The higher voltage at a given current density reflects lower activation and ohmic losses, which can be attributed to the increased number of TPBs. The larger catalyst layer likely enhanced the proton and electron transport. Importantly, the high loading cell maintains a stable performance up to approximately 35 mA/cm^2. This suggests that the high-loading electrode is more robust under high current density, which is likely due to enhanced mass transport properties. While these improvements confirm the benefit of increasing the catalyst loading, it is important to balance the performance gain with material cost. Figure 29 shows the corresponding power density as a function of the current density for the medium- and high-loading electrodes.

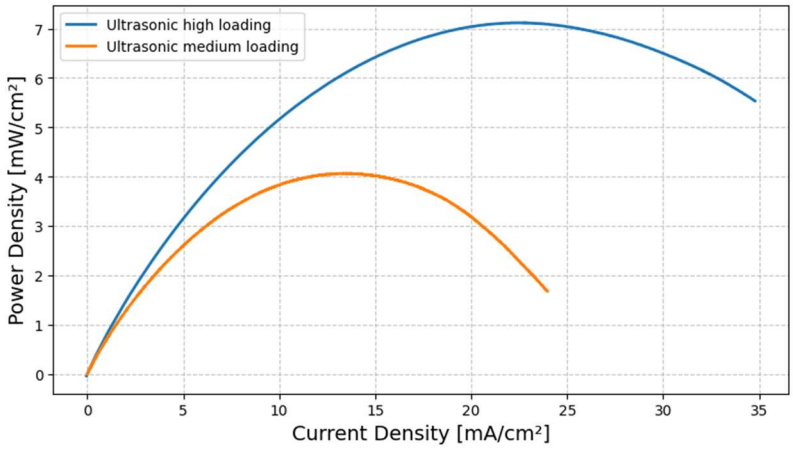

Figure 29: Comparison of power density curves as a function of the current density for ultrasonic with medium loading (0.75 mgPt/cm²) and ultrasonic spray coating with high loading (1.50 mgPt/cm²)

The ultrasonic high-loading electrode performed significantly better than the medium-loading electrode, reaching up to 7.12 mW/cm² at 23.57 mA/cm². This result indicates that doubling the concentration has a positive effect on the power output, especially in the ohmic and mass transport regions. This is possibly due to the increased availability of active catalytic sites within the thicker layer. Additionally, the power output remains stable up to 35 mA/cm², suggesting an increase in durability under load. On the contrary, the medium loading electrode reaches its peak power density at 13.74 mA/cm², after which the performance declines quickly. Due to the smaller catalyst layer, the ECSA is smaller, which means the cell reaches its maximum power density at a lower current density. Overall, the result suggests that increasing the catalyst loading enhances the performance, but not at a 1:1 ratio. The performance gain per unit of added coating becomes smaller because excess material can lead to thicker layers, reduced porosity, and higher resistance; all of which offset the expected benefits.

4.5 Comparison of catalyst usage of each coating technique

In addition to the structural and electrochemical performance of the coatings, practical aspects, such as processing time, ink consumption, losses during coating, and possible scalability, are evaluated across all techniques for a target loading of 0.75 mg_{Pt}/cm^2. Table 3 summarises the coating efficiency as a function of platinum usage, ink volume, and coating duration for target loading.

Table 3: Summary of the practical results of each coating technique for a 0.77 mg_{Pt}/cm^2 coating

Method	Coating duration	Ink volume (ml)	Pt consumed (mg)
Jetting	3	8	6
Ultrasonic spray coating	3	50	37.5
Air spray coating	4	120	90
Hand spray coating	>6	80	60

The result shows a clear trend: techniques that use more Pt to achieve the same loading are associated with higher material losses. This suggests that significant inefficiencies exist in these methods which must be optimised to maintain a low material loss. Jetting, while having a lower maximum power density for the target loading, achieved the most efficient time and Pt usage, reflecting minimal overspray, which is in parallel with the works of Santangelo *et al* [68]. Due to the precise deposition, the method requires a highly levelled and optimally placed substrate and minor disturbances in surface geometry in order to deposit on the fiber of the mesh.

Ultrasonic spray coating presents a well-balanced approach with near full automation and moderate Pt losses. Its duration of three hours and good reproducibility make it a promising candidate for upscaling, despite having more material losses. Air spray coating consumed a significant amount of Pt for reaching the target loading. This is possibly due to the inadequate solvent evaporation during coating. While the time is manageable and the method is used most often for upscaling, the scalability for this application remains questionable, given the significant material waste. Hand spray coating which is the least automated and most operator dependant method, required more than eight hours. It consumed a significant amount of Pt for the given loading and is noticeably difficult to scale or replicate. This makes this method useful for smaller loadings and early-stage screening of new inks.

4.6 Economic feasibility analysis

4.6.1 CAPEX and OPEX

While electrode performance is often the primary focus of PEMFC development, the economic feasibility is of the different coating technologies is equally important for scaling up. This section compares the three methods: air spray coating, ultrasonic spray coating and jetting based on their CAPEX and OPEX, as well as their price per W performance and price per Area of the electrode. These metrics can evaluate both the short- and long-term cost of each technique. Hand spray coating is not included as it is not economically feasible to upscale or automate. Table three shows the important economic factors for upscaling.

Table 4: Summary of the CAPEX and OPEX analysis of coating techniques

Method	CAPEX (€)	OPEX per ca. 0.77 mg_{Pt}/cm^2 (€)	Cost per Watt (€/W)	Cost per Area (€/cm^2)
Jetting	23,500	1.72	113.30	0.30
Ultrasonic spray coating	125,000	8.06	283.96	1.16
Air spray coating	13,500	24.19	786.27	3.67

Jetting achieves the lowest cost per mW produced, making it the most efficient method despite producing lower absolute power output. This due to the precise deposition in combination with the minimal Pt loss, which significantly lower material cost. It also offers a high degree of automation, reducing operator variability and making it an ideal candidate for upscaling. Ultrasonic spray coating yields a medium cost per watt, but this method suffers from extremely high CAPEX. The cost per watt is around ~2.5x higher than jetting. Air spray coating offers a similar CAPEX to jetting but suffers from a very high cost per watt. This is nearly 8x higher than jetting. The cost per area is also dependant on the OPEX, giving similar outcome for each technique regarding the economic feasibility.

4.6.2 Manufacturing scalability considerations

Beyond the €/W, the feasibility of scaling up each technique is an important factor. Jetting is well-suited for scale-up due to its modular nature. Multiple drop-on-demand systems can operate parallel, allowing for the coating of multiple meshes at the same time. At the same time, the CAPEX is lower than the ultrasonic deposition method, allowing for more systems in the same budget.

Although ultrasonic spray coating and air spray coating have been used more for upscaling due to their higher throughput potential and possibly higher coating speeds, this advantage is largely offset by their higher material waste and OPEX, which do not scale in their favour.

Jetting is the most cost-effective method for PEMFC electrode fabrication due to its low CAPEX and OPEX. This makes it the most viable technique for industrial upscaling, especially when reducing Pt consumption and total cost per electrode is crucial.

4.7 Complete summary of results for PEMFC

As a final part of this comparison, the findings of the morphological, economic and practical assessments, Table 5 provides a comparative overview of the key advantages and limitations of each deposition technique. Five evaluation criteria were selected for the final comparison: coating uniformity, material usage, scalability, CAPEX, OPEX and reproducibility. The symbols (++ to --) were used to represent the relative performance, with '++' indicating a strong performance and '—' indicating a clear drawback.

Table 5: Comparative assessment of coating techniques

Method	Coating uniformity	Material usage	Scalability	Cost CAPEX	Cost OPEX	Reproducibility
Jetting	--	++	++	++	++	+
Ultrasonic spray coating	++	+	+	--	+	++
Air spray coating	+	-	+	++	--	+
Hand spray coating	+	--	--	++	--	-

As shown in the table, each technique presents a distinct trade-off between performance, efficiency and practicality. Jetting offers excellent control over material usage and scalability but suffers from poor coating uniformity due to irregular deposition at micro-scale. Ultrasonic spray coating on the other hand delivers the highest coating quality and consistency, though at the expense of higher CAPEX and OPEX. The air spray coating has decent reproducibility, but its scalability is hindered by the high OPEX. Hand spray coating remains the most accessible and low-cost option, though its manual operation hinders the repeatability and scalability.

4.8 Complementary results for SOEC

4.8.1 Ink stability

In order to properly coat the ceramic electrode, the short-term stability of the GDC-CSC suspension is assessed. First, Turbiscan measurements are performed over a six-hour interval. Figure 30 shows the Turbiscan results of both the individual powders and the powders combined, all in the final suspension.

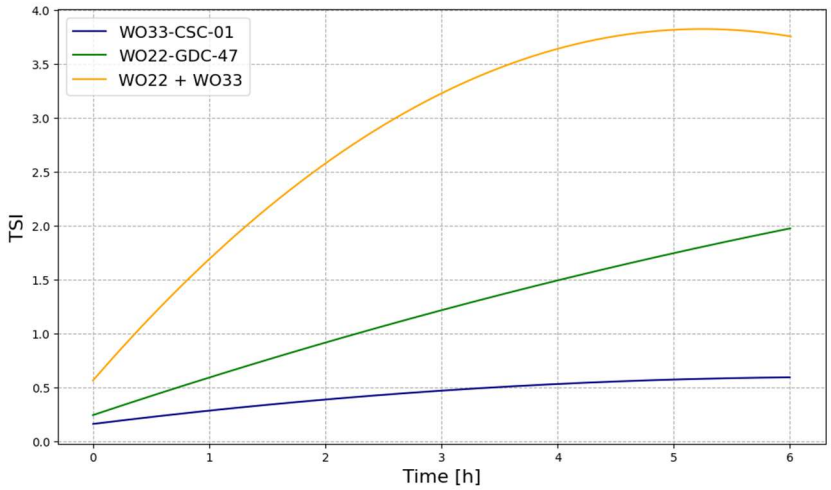

Figure 30: TSI as a function of time for both the individual powders in green and blue and the powders combined in orange

The results demonstrate notable differences in stability between the individual powders and the final suspension. The CSC-only suspension exhibits excellent stability, with a TSI of 0.7 after six hours. In contrast, the GDC suspension shows moderate destabilisation after six hours with a TSI of 2.3. when combining the individual powders, the TSI increases significantly to 4.5 after six hours, indicating a higher sedimentation characteristic when combining the two powders. However, as the suspension is coated within one hour of ultrasonication, this level of instability remains acceptable. Further optimisation to improve the shelf-life of the ceramic ink suspension is outside the scope of this work.

Since the maximum allowable nozzle size for the jetting system is 100 µm, a PSD analysis is conducted on both powders to ensure compatibility with the coater. Figure 35b and 35c in the Appendix present the PSD results of the individual powders. Both contain particles approaching the 100 µm limit, which poses a risk of clogging. To mitigate this, the combined suspension is sieved under a 32 µm mesh. The resulting PSD, shown in Figure 35d in the Appendix, demonstrates a reduction in agglomerates, with particle sizes under 20 µm.

4.8.2 Electrochemical analysis

The Arrhenius plot, which relates the ASR to the inverse of temperature (1000/T), shows how the electrode structure influences electrochemical performance at different temperatures. Figure 31 compares the ASR values for a jetting-coated GDC substrate and an ultrasonic spray-coated GDC substrate.

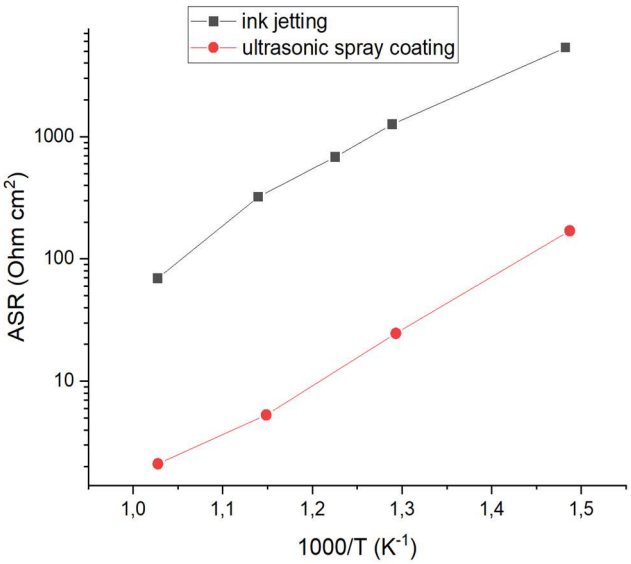

Figure 31: Arrhenius plot shows ASR as a function of inverse temperature for jetting (grey) and ultrasonic spray-coating (red)

Across the full temperature range, the ultrasonic spray-coated samples show a significantly lower ASR, indicating both an improved ionic conduction and electrical performance. On the contrary, the slope of the curve, related to the activation energy, is notably steeper than the jetted samples, suggesting slower kinetics and higher internal resistance. The differences between the two samples likely arise from variations in coating uniformity and porosity introduced by each deposition method. While the Arrhenius plot provides insight in the influence of the temperature on the coated sample, a more detailed understanding of the resistive and capacitive behaviour of the electrodes can be made using EIS. Figure 32 shows the Nyquist plots for both (a) jetting coated and (b) ultrasonic spray-coated electrodes, measured at various temperatures.

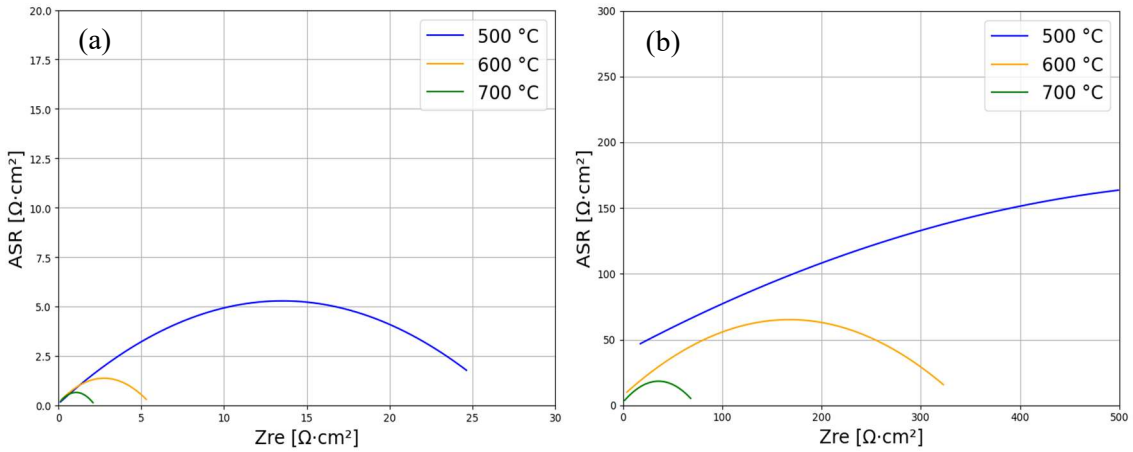

Figure 32: Nyquist plot for (a) jetting and (b) ultrasonic spray coating for 500 °C, 600 °C and 700 °C

From the jetting-coated electrode (a), large semicircle diameters are observed, particularly at 500 °C and 600 °C, indicating significant polarisation resistance. Even at 700 °C, the impedance remains relatively high, suggesting that charge transfer remains hindered across the electrode interface. In contrast, the ultrasonic spray-coated sample (b) showed much smaller semicircles and a far more efficient charge transport. The reduction in both real and imaginary components suggests that there is better contact between the particles and the electrolyte. These results are in line with the Arrhenius plots and confirm that ultrasonic spray coating results in a more conductive and electrochemically favourable electrode coating. Figure 33 provides SEM micrographs comparing the cross-sectional structure of jetting and ultrasonic spray coating samples, both before and after EIS measurements.

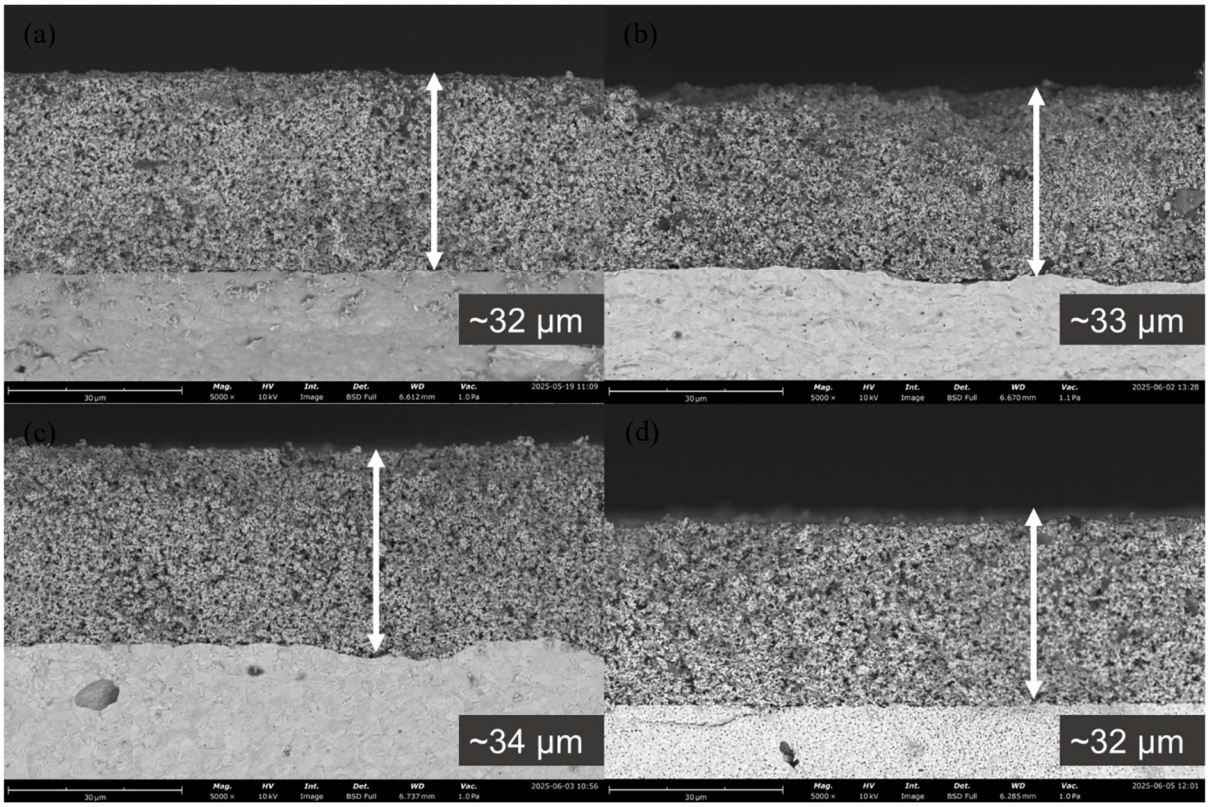

Figure 33: SEM micrograph of (a) jetting before EIS measurement, (b) jetting after EIS measurement, (c) ultrasonic spray coating before EIS and (d) ultrasonic spray coating after EIS

Upon closer analysis, the jetted sample (Figures 33a and 33b) shows visible top-layer degradation after EIS, suggesting degradation and potentially reduced electrochemical stability. In contrast, the ultrasonic spray-coated sample (Figures 33c and 33d) retains its top layer structure after EIS, indicating a more resilient and homogeneous coating. This is possibly due to the increased surface activation due to EIS as seen in the subtle surface roughening. This may have a positive impact on the catalyst accessibility activity and EIS results.

5 Conclusions

Optimising the deposition techniques to reduce Pt consumption without sacrificing performance is essential for making fuel cells economically viable at scale. In this master's thesis, four additive manufacturing are compared to determine which deposition technique offers better control over catalyst distribution, performance and cost.

The motivation behind this comparison lies in the fundamental differences between the techniques. Jetting offers precision through a drop-on-demand system, which reduces material waste. The spray coating methods, except for hand spray coating, are widely used in industry for their simplicity and potential scalability. Hand spray coating is used extensively in R&D. However, due to its ineffectiveness and material consumption, it is rendered unsuitable for scaling up the Fuel Cell technology.

The first step was this study was to develop a stable ink suspension containing Pt supported on KB and Nafion® in IPA/water solvent. Although ink stability alone did not dictate final cell performance, unstable formulations could lead to clogging or non-uniform deposition. Through SMLS and PSD, a final suspension, containing both 1.5 mg/ml Pt/C and 1.5 mg/ml Nafion® in 80/20 IPA/water offered sufficient shelf life, good stability and hence suitability for each coating system.

Morphological characterisation through SEM and EDS provides clear differences between the deposition techniques, both in structural uniformity and catalyst distribution. The air spray deposition method generates a visibly porous layer with larger irregular spaces, indicating a less efficient deposition. This can be attributed to inadequate spray control during deposition, which results in higher surface wetting. The hand spray method showed an improved uniformity and porosity. The voids are smaller and more evenly distributed, likely due to the lower coating flow rate. The jetting technique creates significant channelled voids and variable coating thickness with ink penetrating the pores of the 3D printed mesh. These issues link to the nozzle pressure build-up between the coating cycles, which creates a blockage for the Pt/C particles. This problem can be resolved by increasing the pressure before starting the coating cycle. Ultrasonic spray coating results in the most uniform, uniform in thickness and has minimal voids. The fine atomisation contributes to marked improvements when compared to the other techniques.

These morphological differences are further confirmed by EDS elemental mapping. The air spray coating deposition method has the most uneven Pt distribution, with areas of heavy clustering interspersed with regions that lack a Pt signal, which mirrors the SEM micrography. The hand spray coating provides a more continuous Pt layer, but agglomeration of Pt particles is still visible. The jetting technique produced an irregular Pt distribution with deeply embedded, Pt-rich regions combined with large voids, which points to the unstable droplet concentration during deposition. In contrast, ultrasonic spray coating produced a dense, continuous well-distributed Pt signal which confirms the findings from the SEM micrography.

The performance evaluation of the PEMFC electrodes provides insight into the electrochemical behaviour of each coated layer. Among the four methods, hand spray-coated is excluded from the performance testing due to its limitations in scalability and reproducibility. The operator-dependant nature of the coating method makes it more time-consuming and less reproducible, which prevents efficient scale-up. For the three main coating methods, voltage and power density as a function of current density were measured. Firstly, maximum power density of the medium-loaded samples (ca. 0.77 mg/cm^2) demonstrated that ultrasonic spray coating achieved the highest peak power density at low to moderate current densities, which indicates a well-balanced electrode with efficient activation and

moderate ohmic losses. Jetting gave the best performance at low current densities but suffered from high ohmic and mass transport losses, possibly due to the large voids of the non-uniform layer, observed in the SEM micrography. The performance of the air spray-coated sample is hindered firstly by high activation losses. However, its more porous morphology proved advantageous in the mass transport region, allowing it to surpass the other techniques at higher current densities and provide the highest peak power density.

When comparing the medium and high catalyst loading for ultrasonic spray coating, it is evident that increasing the load to 1.50 mg_{Pt}/cm^2 leads to significant improvements overall current densities. The increase in available TPBs leads to an overall improvement of the cell. Nevertheless, the performance gain is not linear with catalyst usage. Doubling the layer thickness does not double the power output, which indicates potential diffusion limitations, highlighting the importance of balancing performance improvements with material efficiency.

In addition to the electrochemical performance, practical and economic considerations determine the suitability of each coating technique or upscaling. Jetting proves to be the most efficient in Pt consumption and coating time, having achieved the target loading with minimal losses. This is due to the precise control and minimal overspray, making it well-suited for upscaling. Although its absolute maximum power density is lower, the reduced Pt use results in the lowest cost per watt and the lower OPEX per coated unit, positioning jetting as the most economically attractive option overall. Ultrasonic spray coating offers a good performance and great coating quality but suffers from high Pt losses and operating costs. This is accompanied by the highest CAPEX due to specialised equipment needed for the fine atomisation. Air spray coating suffers from excessive Pt waste, generating high OPEX, leading to the highest cost per watt. This raises concerns regarding the economic scalability of this technology. Hand spray coating, although inexpensive and useful for low loading prototyping, is excluded as its does not fit the scalability criteria.

Taken together, the results demonstrate that each deposition technique offers a unique combination of strengths and weaknesses, requiring a balance between coating performance, resource efficiency and economic feasibility. Jetting stands out in terms of material usage and scalability opportunities but remains limited by its coating uniformity due to droplet inconsistencies. Despite this limitation, it is the most cost-efficient per watt, making it a good contender for scaling up PEMFC electrode production. Ultrasonic spray coating performs best in terms of coating quality and reproducibility. However, its high CAPEX and moderate Pt losses pose financial challenges for industrial implementation. Air spray coating offers the highest peak power density but suffers from high OPEX and inefficient Pt usage, which severely limits its competitiveness in application where material usage is crucial. Ultimately, no single deposition method can be considered ideal in all categories. The optimal technique depends on the intended purpose, whether the priority is maximum performance, high coating uniformity or economic viability in a scaling production environment.

For the complementary results, the SEM analysis and EIS measurements confirm that ultrasonic spray coating produces a more stable and homogeneous electrode structure compared to jetting. Post-EIS SEM micrography reveals notable surface roughness and degradation in the coated electrode, made using jetting. The ultrasonic-coated electrode maintained its structural integrity, suggesting improved electrochemical durability. These findings align with the Arrhenius and Nyquist results, reinforcing that ultrasonic spray coating yields coatings that are both electrochemically favourable and mechanically resilient, making it better for this SOEC application than jetting. Overall, this complementary research demonstrated that both jetting and ultrasonic spray coating are adaptable across electrochemical systems, reinforcing their potential for scalable, multipurpose application

Acknowledgments

The work on coating SOEC electrodes was partially funded by the European Union's Horizon Europe Programme, project NOUVEAU, under grant agreement number N°101058784. The present work reflects only the author’s views and the European Union is not liable for any use that may be made of the information contained therein.

References

[1] K. Li and B. Lin, “Impacts of urbanization and industrialization on energy consumption/CO2 emissions: Does the level of development matter?,” *Renewable and Sustainable Energy Reviews*, vol. 52, pp. 1107–1122, 2015, doi: https://doi.org/10.1016/j.rser.2015.07.185.

[2] M. Dayarathna, Y. Wen, and R. Fan, “Data center energy consumption modeling: A survey,” *IEEE Communications Surveys and Tutorials*, vol. 18, no. 1, pp. 732–794, Jan. 2016, doi: 10.1109/COMST.2015.2481183.

[3] B. Paul and J. Andrews, “PEM unitised reversible/regenerative hydrogen fuel cell systems: State of the art and technical challenges,” *Renewable and Sustainable Energy Reviews*, vol. 79, pp. 585–599, 2017, doi: https://doi.org/10.1016/j.rser.2017.05.112.

[4] S. Sorrell, “Reducing energy demand: A review of issues, challenges and approaches,” *Renewable and Sustainable Energy Reviews*, vol. 47, pp. 74–82, 2015, doi: https://doi.org/10.1016/j.rser.2015.03.002.

[5] D. Coleman, “The shape of things to come: world population to 2050,” in *In Empire and the Future. World Order: perspectives from the Engelsberg seminar 2005.*, Almqvist K and Thomas I, Eds., Stockholm: Axel and Margaret Ax:son Johnson Foundation, 2007, pp. 209–230.

[6] P. Sharma and O. P. Pandey, “Proton exchange membrane fuel cells: Fundamentals, advanced technologies, and practical applications,” in *PEM Fuel Cells: Fundamentals, Advanced Technologies, and Practical Application*, Elsevier, 2021, pp. 1–24. doi: 10.1016/B978-0-12-823708-3.00006-7.

[7] P. Cook, “Infrastructure, rural electrification and development,” *Energy for Sustainable Development*, vol. 15, no. 3, pp. 304–313, 2011, doi: https://doi.org/10.1016/j.esd.2011.07.008.

[8] V. Malik, S. Srivastava, M. K. Bhatnagar, and M. Vishnoi, “Comparative study and analysis between Solid Oxide Fuel Cells (SOFC) and Proton Exchange Membrane (PEM) fuel cell - A review,” in *Materials Today: Proceedings*, Elsevier Ltd, 2021, pp. 2270–2275. doi: 10.1016/j.matpr.2021.04.203.

[9] Sammes M. Nigel, Bove Roberto, and Pusz Jakub, “Solid oxide Fuel cells,” in *Fuel Cell Technology: Reaching Towards Commercialisation*, B. Derby and Nigel M. Sammes, Eds., Colorado: Springer London, 2006, ch. 1, pp. 1–26. doi: 10.1007/1-84628-207-1.

[10] S. Pérez-Rodríguez, E. Pastor, and M. J. Lázaro, “Electrochemical behavior of the carbon black Vulcan XC-72R: Influence of the surface chemistry,” *Int J Hydrogen Energy*, vol. 43, no. 16, pp. 7911–7922, Apr. 2018, doi: 10.1016/j.ijhydene.2018.03.040.

[11] “Carbon Black - Ketjenblack EC-300J SKU: 52080001.” Accessed: Apr. 03, 2025. [Online]. Available: https://www.fuelcellstore.com/ketjenblack-carbon-black-ec300j?

[12] Md. M. Rahman *et al.*, “Synthesis of catalysts with fine platinum particles supported by high-surface-area activated carbons and optimization of their catalytic activities for polymer electrolyte fuel cells,” *RSC Adv*, vol. 11, no. 33, pp. 20601–20611, 2021, doi: 10.1039/D1RA02156G.

[13] M. S. Habib *et al.*, “Proton Exchange Membrane Fuel Cell (PEMFC) Durability Factors, Challenges, and Future Perspectives: A Detailed Review,” *Material Science Research India*, vol. 18, no. 2, pp. 217–234, Aug. 2021, doi: 10.13005/msri/180209.

[14] F. A. De Bruijn, “PEM Fuel Cells Durability and Cost,” in *Hydrogen and Fuel Cells in the Nordic Countries 2009*, Oslo, Nov. 2009, pp. 1–46.

[15] A. Ali, A. Al-Othman, and M. Tawalbeh, “Grand Challenges in Fuel cell Technology towards Resource Recovery,” *Journal of Resource Recovery*, vol. 1, Jan. 2023, doi: 10.52547/jrr.2211.1004.

[16] L. Marsili, Randlhofer Gabriele, C. Heron, and F. Capon, “Joint briefing note Platinum Group Metals (PGMs)-essential critical raw minerals for the hydrogen economy IEA Critical Minerals and Clean Energy Summit,” Paris, Sep. 2023. [Online]. Available: https://hydrogeneurope.eu/wp-content/uploads/2022/12/2022.12_HE-and-ACEA-letter-on-

[17] K. Mochizuki, T. Kikuchi, M. Sudoh, Y. Ishiguro, and T. Suzuki, “Comparison between Nafion and Polybenzimidazole (PBI) Membranes for Fuel Cell Type CO Sensor,” in *The Electrochemical Society*, vol. 28, The Electrochemical Society, 2010, pp. 91–99. doi: 10.1149/1.3489935.

[18] Y. Chen *et al.*, “Feasibility of using thin polybenzimidazole electrolytes in high-temperature proton exchange membrane fuel cells,” *Int J Hydrogen Energy*, vol. 47, no. 66, pp. 28615–28625, Aug. 2022, doi: 10.1016/j.ijhydene.2022.06.156.

[19] S. Vafaeyan, A. St-Amant, and M. Ternan, “Nickel Alloy Catalysts for the Anode of a High Temperature PEM Direct Propane Fuel Cell,” *J Chem*, vol. 2014, no. 1, p. 151638, Jan. 2014, doi: https://doi.org/10.1155/2014/151638.

[20] G. M. Sisó, *Thesis for the Degree of Doctor of Philosophy Electrocatalyst Materials for Low-Temperature Hydrogen Fuel Cells*. Gothenburg, 2023.

[21] M. Bayat, S. Kaskun Ergani, Y. Daşdemirli, and M. Kayfeci, “Fuel cells basics and types,” in *Handbook of Thermal Management Systems: E-Mobility and Other Energy Applications*, Elsevier, 2023, pp. 371–399. doi: 10.1016/B978-0-443-19017-9.00019-2.

[22] D. Ali, “Hydrogen Fuel Cell Technology,” *Journal of Chemistry & its Applications*, pp. 1–7, Sep. 2023, doi: 10.47363/JCIA/2023(2)121.

[23] “Diving into the types of Hydrogen: Green, Blue, Grey and Other Types of Hydrogen Explained .” Accessed: Apr. 09, 2025. [Online]. Available: https://stargatehydrogen.com/blog/types-of-hydrogen/

[24] “CUSTOM MEMBRANE ELECTRODE ASSEMBLIES.” Accessed: Apr. 18, 2025. [Online]. Available: https://fuelcellsetc.com/membrane-electrode-assemblies/

[25] H. Liu, P. Li, D. Juarez-Robles, K. Wang, and A. Hernandez-Guerrero, “Experimental Study and Comparison of Various Designs of Gas Flow Fields to PEM Fuel Cells and Cell Stack Performance,” *Front Energy Res*, vol. 2, 2014, doi: 10.3389/fenrg.2014.00002.

[26] J. W. Weidner, V. A. Sethuraman, and J. W. Van Zee, “The Electrochemical Society INTERFACE: Engineering a Membrane Electrode Assembly,” 2003. doi: 10.1149/issn.1944-8783.

[27] D. Ye and Z. Zhan, “A review on the sealing structures of membrane electrode assembly of proton exchange membrane fuel cells,” *J Power Sources*, vol. 231, pp. 285–292, Jun. 2013, doi: 10.1016/j.jpowsour.2013.01.009.

[28] N. A. A. Qasem and G. A. Q. Abdulrahman, “A Recent Comprehensive Review of Fuel Cells: History, Types, and Applications,” 2024, *Wiley-Hindawi*. doi: 10.1155/2024/7271748.

[29] U. Lucia, “Overview on fuel cells,” 2014, *Elsevier Ltd*. doi: 10.1016/j.rser.2013.09.025.

[30] “Fuel Cell Technologies: State and Perspectives.” [Online]. Available: http://www.nato.int/science

[31] Barbir Frano, “PEM Fuel Cells,” in *Fuel Cell Technology: Reaching Towards Commercialisation*, Sammes Nigel and Derby B, Eds., Coleardo: Springer-Verlag, 2006, pp. 27–52.

[32] O. T. Holton and J. W. Stevenson, “The role of platinum in proton exchange membrane fuel cells,” Oct. 2013. doi: 10.1595/147106713X671222.

[33] V. M. Vishnyakov, “Proton exchange membrane fuel cells,” *Vacuum*, vol. 80, no. 10, pp. 1053–1065, 2006, doi: https://doi.org/10.1016/j.vacuum.2006.03.029.

[34] F. Xiao *et al.*, “Recent Advances in Electrocatalysts for Proton Exchange Membrane Fuel Cells and Alkaline Membrane Fuel Cells,” *Advanced Materials*, vol. 33, no. 50, p. 2006292, 2021, doi: https://doi.org/10.1002/adma.202006292.

[35] J.-H. Wee, “Applications of proton exchange membrane fuel cell systems,” *Renewable and Sustainable Energy Reviews*, vol. 11, no. 8, pp. 1720–1738, 2007, doi: https://doi.org/10.1016/j.rser.2006.01.005.

[36] “Polarization Curves.” Accessed: Apr. 20, 2025. [Online]. Available: https://www.fuelcellstore.com/blog-section/fuel-cell-information/polarization-curves

[37] D. Van Dao, G. Adilbish, T. D. Le, I.-H. Lee, and Y.-T. Yu, “Triple phase boundary and power density enhancement in PEMFCs of a Pt/C electrode with double catalyst layers,” *RSC Adv*, vol. 9, no. 27, pp. 15635–15641, 2019, doi: 10.1039/C9RA01741K.

[38] M. I. Khan, A. Shanableh, S. Shahida, M. H. Lashari, S. Manzoor, and J. Fernandez, “SPEEK and SPPO Blended Membranes for Proton Exchange Membrane Fuel Cells,” *Membranes (Basel)*, vol. 12, no. 3, Mar. 2022, doi: 10.3390/membranes12030263.

[39] N. Shaari *et al.*, “Recent advances and fundamentals of polymer electrolyte membrane in direct borohydride fuel cell application: Effectiveness, reliability, degradation, and mitigation strategies,” Nov. 04, 2024, *Elsevier Ltd*. doi: 10.1016/j.ijhydene.2024.09.249.

[40] J. A. Kilner, J. Druce, and T. Ishihara, “Electrolytes,” in *High-Temperature Solid Oxide Fuel Cells for the 21st Century: Fundamentals, Design and Applications*, Elsevier, 2015, pp. 85–132. doi: 10.1016/B978-0-12-410453-2.00004-X.

[41] F. Zishan, O. D. Montoya, and D. A. Giral-Ramírez, “New Design and Study of the Transient State and Maximum Power Point Tracking of Solid Oxide Fuel Cells Using Fuzzy Control,” *Energies (Basel)*, vol. 16, no. 6, p. 2572, Mar. 2023, doi: 10.3390/en16062572.

[42] T. Kawada and T. Horita, “Cathodes,” in *High-Temperature Solid Oxide Fuel Cells for the 21st Century: Fundamentals, Design and Applications*, Elsevier, 2015, pp. 161–193. doi: 10.1016/B978-0-12-410453-2.00006-3.

[43] M. Cassidy, P. A. Connor, J. T. S. Irvine, and C. D. Savaniu, “Anodes,” in *High-Temperature Solid Oxide Fuel Cells for the 21st Century: Fundamentals, Design and Applications*, Elsevier, 2015, pp. 133–160. doi: 10.1016/B978-0-12-410453-2.00005-1.

[44] S. Y. Gómez and D. Hotza, “Current developments in reversible solid oxide fuel cells,” Aug. 01, 2016, *Elsevier Ltd*. doi: 10.1016/j.rser.2016.03.005.

[45] M. Kusnezoff, N. Trofimenko, M. Müller, and A. Michaelis, “Influence of electrode design and contacting layers on performance of electrolyte supported SOFC/SOEC single cells,” Nov. 01, 2016, *MDPI AG*. doi: 10.3390/ma9110906.

[46] Q. Liang *et al.*, “Effect of MgO and Fe2O3 dual sintering aids on the microstructure and electrochemical performance of the solid state Gd0.2Ce0.8O2-δ electrolyte in intermediate-temperature solid oxide fuel cells,” *Front Chem*, vol. 10, Sep. 2022, doi: 10.3389/fchem.2022.991922.

[47] B. Hua, M. Li, B. Chi, and L. Jian, “Enhanced electrochemical performance and carbon deposition resistance of Ni–YSZ anode of solid oxide fuel cells by in situ formed Ni–MnO layer for CH $_4$ on-cell reforming,” *J. Mater. Chem. A*, vol. 2, no. 4, pp. 1150–1158, 2014, doi: 10.1039/C3TA12766D.

[48] D. John and A. Hutton, “6.2.3.4: The Arrhenius Law-Arrhenius Plots ‘Linearized’ Arrhenius Equation,” ChemLibreTexts. Accessed: Jun. 06, 2025. [Online]. Available: https://chem.libretexts.org/Bookshelves/Physical_and_Theoretical_Chemistry_Textbook_Maps/Supplemental_Modules_(Physical_and_Theoretical_Chemistry)/Kinetics/06%3A_Modeling_Reaction_Kinetics/6.02%3A_Temperature_Dependence_of_Reaction_Rates/6.2.03%3A_The_Arrhenius_Law/6.2.3.04%3A_The_Arrhenius_Law_-_Arrhenius_Plots#:~:text=3.4%3A%20The%20Arrhenius%20Law%20%2D%20Arrhenius%20Plots,-Last%20updated%20Feb&text=The%20activation%20energy%2C%20Ea,to%20find%20the%20activation%20energy.

[49] Q. Zhao, T. Morawietz, P. Gazdzicki, and K. A. Friedrich, “Strategy to tune properties of PEM fuel cell electrodes with low Pt loading based on inkjet printing parameters,” *J Power Sources*, vol. 625, Jan. 2025, doi: 10.1016/j.jpowsour.2024.235624.

[50] J. Yi *et al.*, “Characterizations and Inkjet Printing of Carbon Black Electrodes for Dielectric Elastomer Actuators,” *ACS Appl Mater Interfaces*, vol. 15, no. 35, pp. 41992–42003, Sep. 2023, doi: 10.1021/acsami.3c05444.

[51] D. Mitra *et al.*, “Direct deposition of catalyst layers on polymer electrolyte membrane (PEM) for fuel cells with controlled platinum distribution by inkjet printing,” *J Power Sources*, vol. 638, p. 236503, May 2025, doi: 10.1016/j.jpowsour.2025.236503.

[52] A. Hussain, N. Abbas, and A. Ali, “Inkjet Printing: A Viable Technology for Biosensor Fabrication,” *Chemosensors*, vol. 10, no. 3, p. 103, Mar. 2022, doi: 10.3390/chemosensors10030103.

[53] H. Hu and R. G. Larson, “Marangoni Effect Reverses Coffee-Ring Depositions,” *J Phys Chem B*, vol. 110, no. 14, pp. 7090–7094, Apr. 2006, doi: 10.1021/jp0609232.

[54] F. A. de Bruijn, V. A. T. Dam, and G. J. M. Janssen, “Review: Durability and Degradation Issues of PEM Fuel Cell Components,” *Fuel Cells*, vol. 8, no. 1, pp. 3–22, Feb. 2008, doi: 10.1002/fuce.200700053.

[55] L. Mesecke, I. Meyer, M. Oel, and R. Lachmayer, “Challenges and potentials for additive manufacturing of hydrogen energy components: A review,” *Int J Hydrogen Energy*, vol. 113, pp. 198–219, Mar. 2025, doi: 10.1016/j.ijhydene.2025.02.441.

[56] X. Deng *et al.*, “Recent Progress in Materials Design and Fabrication Techniques for Membrane Electrode Assembly in Proton Exchange Membrane Fuel Cells,” *Catalysts*, vol. 15, no. 1, Jan. 2025, doi: 10.3390/catal15010074.

[57] F. L. Deschamps *et al.*, “A practical method to characterize proton exchange membrane fuel cell catalyst layer topography: Application to two coating techniques and two carbon supports,” *Thin Solid Films*, vol. 695, p. 137751, Feb. 2020, doi: 10.1016/j.tsf.2019.137751.

[58] K. Talukdar *et al.*, “Exploring critical parameters of electrode fabrication in polymer electrolyte membrane fuel cells,” *J Power Sources*, vol. 540, p. 231638, Aug. 2022, doi: 10.1016/j.jpowsour.2022.231638.

[59] T. Carey, C. Jones, F. Le Moal, D. Deganello, and F. Torrisi, “Spray-Coating Thin Films on Three-Dimensional Surfaces for a Semitransparent Capacitive-Touch Device,” *ACS Appl Mater Interfaces*, vol. 10, no. 23, pp. 19948–19956, Jun. 2018, doi: 10.1021/acsami.8b02784.

[60] C. Girotto, B. P. Rand, J. Genoe, and P. Heremans, “Exploring spray coating as a deposition technique for the fabrication of solution-processed solar cells,” *Solar Energy Materials and Solar Cells*, vol. 93, no. 4, pp. 454–458, Apr. 2009, doi: 10.1016/j.solmat.2008.11.052.

[61] T.-H. Huang, H.-L. Shen, T.-C. Jao, F.-B. Weng, and A. Su, “Ultra-low Pt loading for proton exchange membrane fuel cells by catalyst coating technique with ultrasonic spray coating machine,” *Int J Hydrogen Energy*, vol. 37, no. 18, pp. 13872–13879, Sep. 2012, doi: 10.1016/j.ijhydene.2012.04.108.

[62] Z. Turtayeva *et al.*, “Manufacturing catalyst-coated membranes by ultrasonic spray deposition for PEMFC: Identification of key parameters and their impact on PEMFC performance,” *Int J Hydrogen Energy*, vol. 47, no. 36, pp. 16165–16178, Apr. 2022, doi: 10.1016/j.ijhydene.2022.03.043.

[63] M. B. Sassin, Y. Garsany, B. D. Gould, and K. E. Swider-Lyons, “Fabrication Method for Laboratory-Scale High-Performance Membrane Electrode Assemblies for Fuel Cells,” *Anal Chem*, vol. 89, no. 1, pp. 511–518, Jan. 2017, doi: 10.1021/acs.analchem.6b03005.

[64] M. Wang *et al.*, “Impact of Catalyst Ink Dispersing Methodology on Fuel Cell Performance Using in-Situ X-ray Scattering,” *ACS Appl Energy Mater*, vol. 2, no. 9, pp. 6417–6427, Sep. 2019, doi: 10.1021/acsaem.9b01037.

[65] C. Liu *et al.*, “Performance enhancement of PEM electrolyzers through iridium-coated titanium porous transport layers,” *Electrochem commun*, vol. 97, pp. 96–99, Dec. 2018, doi: 10.1016/j.elecom.2018.10.021.

[66] R. Liu, W. Zhou, W. Ling, S. Li, and F. Li, “Performance optimization of ultra-low platinum loading membrane electrode assembly prepared by electrostatic spraying,” *Int J Hydrogen Energy*, vol. 46, no. 17, pp. 10457–10467, Mar. 2021, doi: 10.1016/j.ijhydene.2020.12.127.

[67] J. Yi *et al.*, “Characterizations and Inkjet Printing of Carbon Black Electrodes for Dielectric Elastomer Actuators,” *ACS Appl Mater Interfaces*, vol. 15, no. 35, pp. 41992–42003, Sep. 2023, doi: 10.1021/acsami.3c05444.

[68] P. Santangelo, M. Cannio, and M. Romagnoli, “Review of Catalyst-deposition Techniques for PEMFC Electrodes,” *TECNICA ITALIANA-Italian Journal of Engineering Science*, vol. 63, no. 1, pp. 65–72, Mar. 2019, doi: 10.18280/ti-ijes.630109.

Appendix

Appendix A

Manual:

1. Basic G-code file upload
2. Run code
3. Add botom text above the itterations
4. Bottom text at the end

```
[ ]  import time
```

```
; Circular Mesh Snake Pattern G-code
; Diameter: 25 mm
; Number of Lines: 64 (per cycle)
; Line Spacing: 0.4 mm
; Speed: 2000 mm/min (~16 mm/s)

G21 ; Set units to millimeters
G90 ; Absolute positioning
G28 ; Home all axes
G1 X0 Y0 Z0 ; Move to start position
G1 Z0.2 F300 ; Move to safe Z height
G1 X95 Y100 F1500 ; Move to start of first line

; Generate snake pattern
M117 Moving Circular Path
G1 F1000 ; Set speed
G4 P2000
```

```
def repeat_gcode(input_file, output_file, iterations=5):
    with open(input_file, 'r') as f:
        gcode_lines = f.readlines()

    header = []
    body = []
    header_done = False

    for line in gcode_lines:
        if line.startswith("G1") or line.startswith("M"):
            header_done = True

        if not header_done:
            header.append(line)
        else:
            body.append(line)

    start_position = None
    for line in body:
        if line.startswith("G1"):
            start_position = line
            break

    with open(output_file, 'w') as f:
        f.writelines(header)
        for i in range(iterations):
            f.write(f"(Iteratie {i+1})\n")
            f.writelines(body)
            if start_position:
                f.write(start_position)

    print(f"G-code succesvol gegenereerd: {output_file}")


input_gcode = "BASIC_0,4_CODE_PEMFC.gcode"
output_gcode = "circular_0,4mm_5_Itteration_PEMFC.gcode"
repeat_gcode(input_gcode, output_gcode)
```

```
G-code succesvol gegenereerd: circular_0,4mm_5_Itteration_SOFC.gcode
```

```
G4 P5000 G1 X0 Y0
```

Figure 34: Python code for semi-optimising the jetting coating cycle

Appendix B

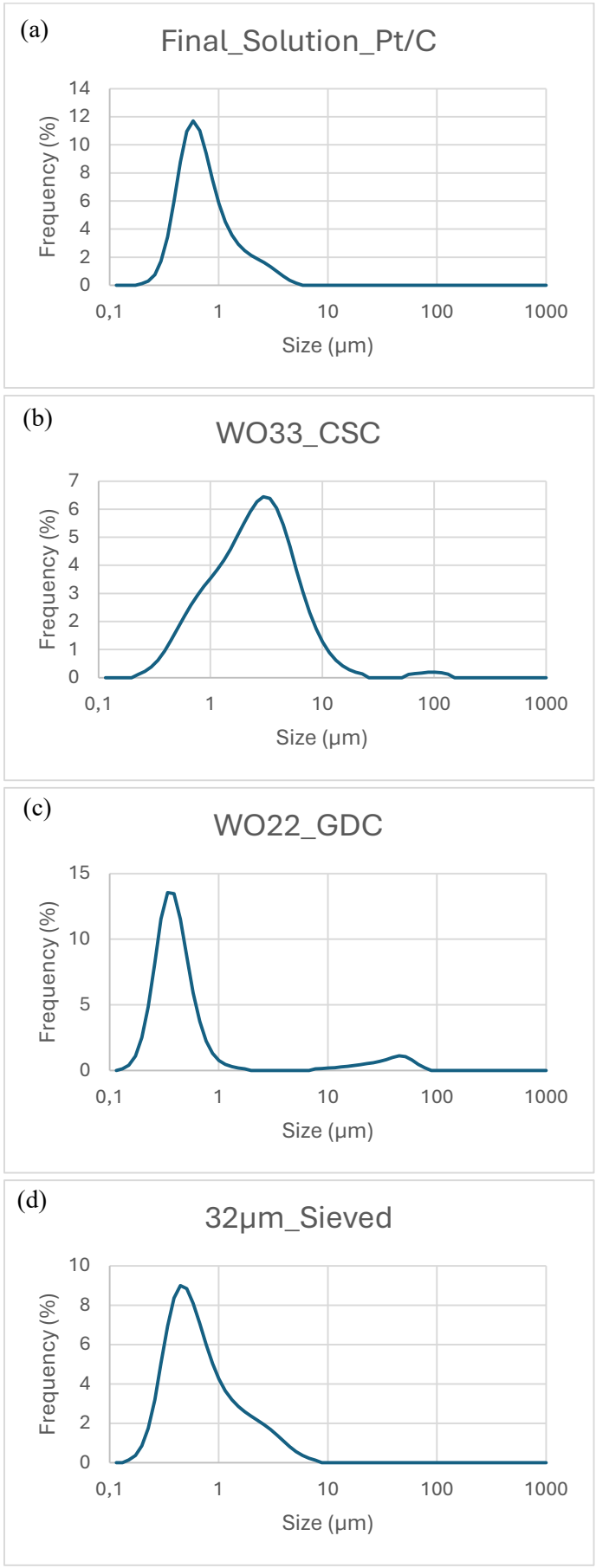

Figure 35: PSD results for each type of ink used in this research

Appendix C

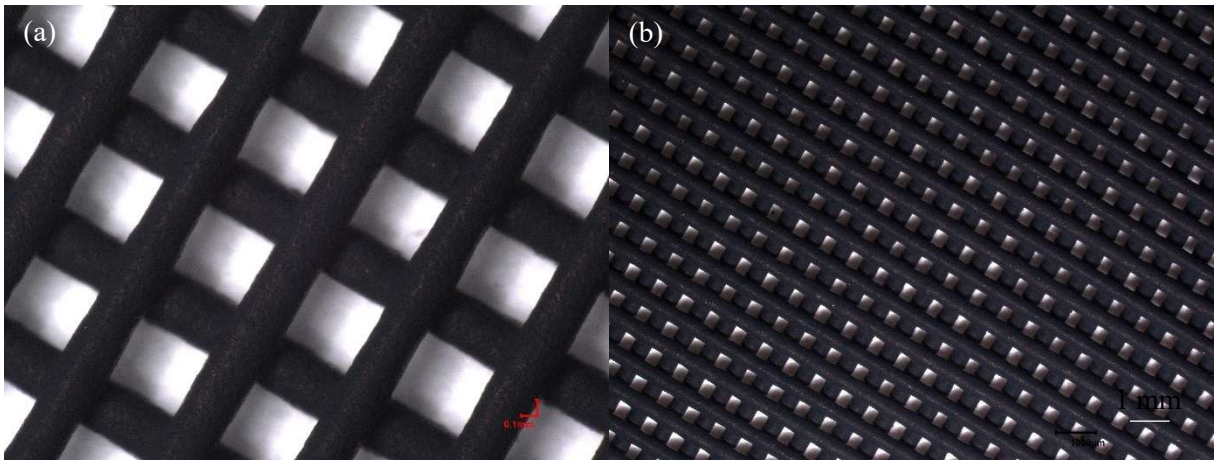

Figure 36: Optical microscopy results showing (a) a jetted sample at 80x and (b) a jetted sample at 20x

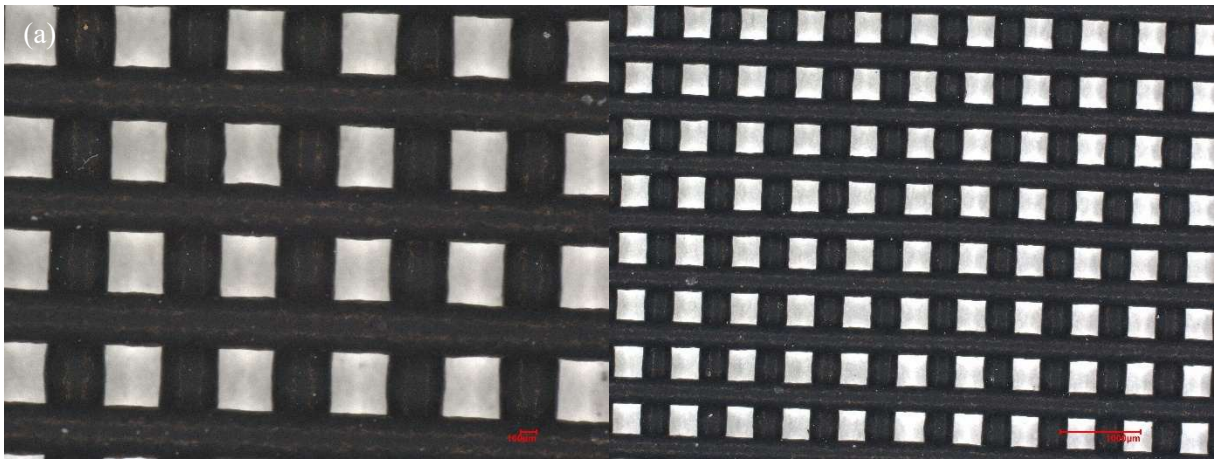

Figure 37: Optical microscopy results showing (a) a ultrasonic spray-coated sample at 80x and (b) an ultrasonic spray-coated sample at 20x

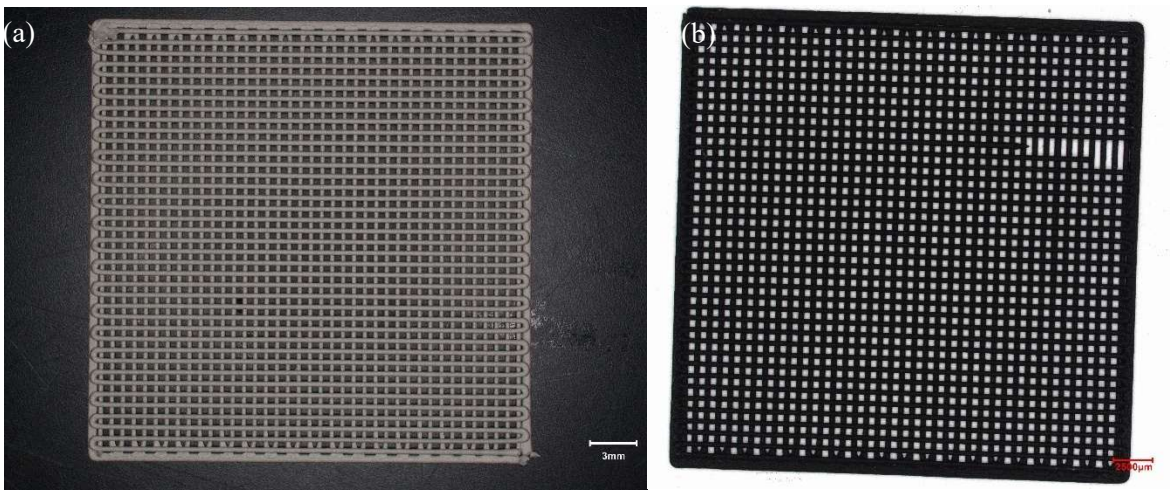

Figure 38: Showing the visual difference between (a) an uncoated and (b) a coated mesh at 5x

Appendix D

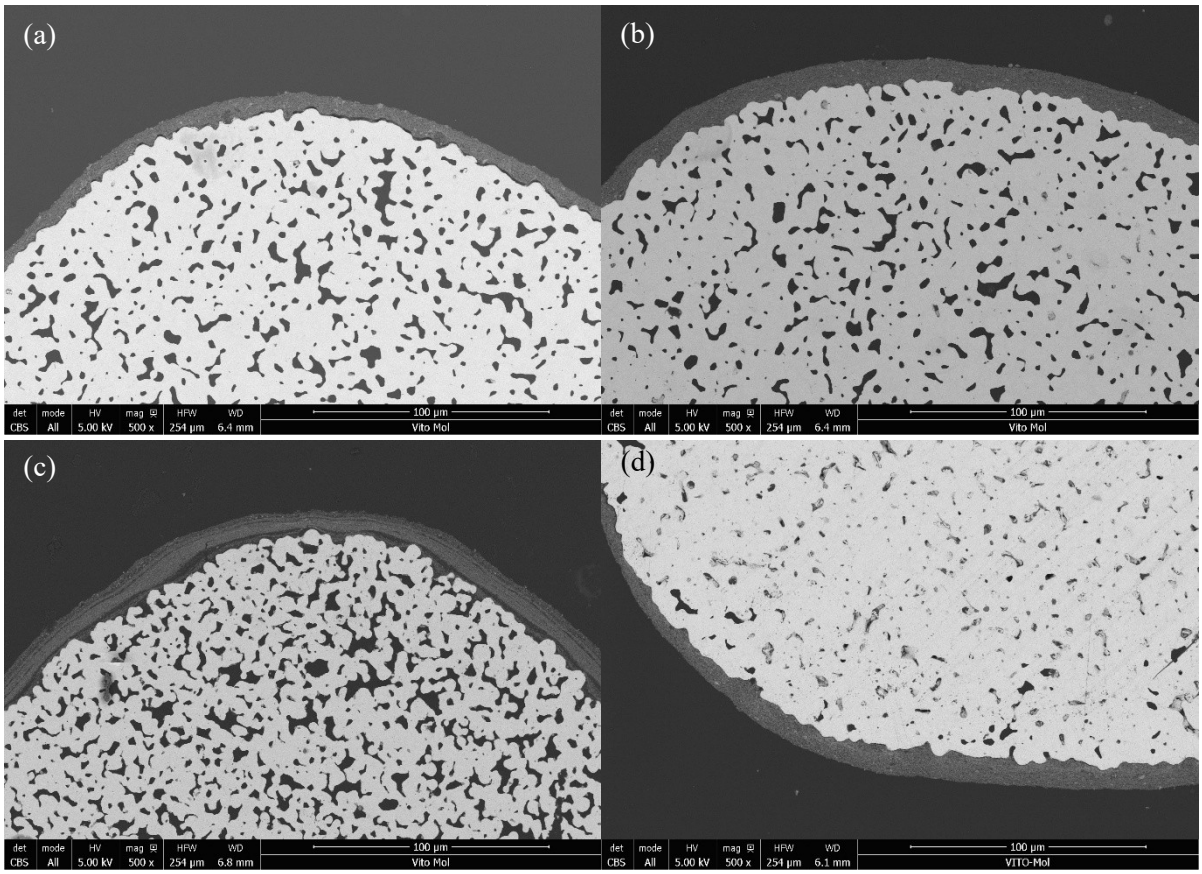

Figure 39: Cross-sectional SEM micrograph of 3D printed meshes, coated with each technique: (a) air spray coating, (b) hand spray coating, (c) jetting and (d) ultrasonic spray coating. All images were captured at 2500x at HV of 5 kV